BUBBLE COALESCENCE DURING DIRECTED ENERGY DEPOSITION OF METALS USING HIGH-SPEED IN-SITU X-RAY IMAGING AND INFRARED THERMOGRAPHY

A Thesis

by

KARAN VINOD KANKARIA

Submitted to the Graduate and Professional School of
Texas A&M University
in partial fulfillment of the requirements for the degree of

MASTER OF SCIENCE

Chair of Committee,	Sarah Wolff
Committee Members,	Shiren Wang
	James Paramore
Head of Department,	Natarajan Gautam

December 2021

Major Subject: Industrial and Systems Engineering

ABSTRACT

The influence of input parameters on the coalescence of bubbles during Directed Energy Deposition of metals is studied. Additionally, the in-situ infrared images captured during the process were dynamically calibrated using the surface temperature at the boundary of the melt-pool and a temperature scaling factor.

Porosity is a key obstacle in the qualification and certification of metal additive manufactured parts. Previous researchers have quantified the effect of porosity on part performance for parts created using directed energy deposition, formation mechanisms of porosity and the effect of process parameters on final part porosity. However, due to the complex system of heat and mass flow in the melt pool, there is limited research that discusses the morphological evolution of the bubbles inside the melt pool. This work uses the in-situ X-ray and IR images taken by Dr. Wolff and her colleagues at the Argonne National Laboratory and analyses the morphological changes that bubbles undergo before the solidification front makes them into final part pores. Coalescence of bubbles is the most profound change that leads to the formation of large pores. Coalescence occurs both leading the laser keyhole and trailing it. It is found that the final part porosity originated mostly in the wake of the keyhole. Additionally, the partially fused powders from the first track, increase the magnitude of the bubbles formed during the second track, which results in more instances of coalescence. Porosity due to instability at tip of the keyhole does not create dense clusters of bubbles required for bubble coalescence.

In-situ thermal imaging of a complex and stochastic process such as DED is indispensable, however, using IR cameras for this purpose can be challenging as the emissivity of the substrate is not constant. One of the observations made in this research was a difference in the magnitude and direction of the change in emissivity between the first track and the second track. The emissivity values were higher for the second track and further investigation into this shall be done in the future.

DEDICATION

I dedicate this work to my parents for their lifelong support to my education and belief in my work.

ACKNOWLEDGMENTS

I thank Dr. Sarah Wolff for teaching me about metal additive manufacturing. I am thankful for the experiments conducted by the her collegues that enabled me to pursue my research. Dr. Hui Wang and Marwan Haddad have been very helpful and have made this journey easier.

CONTRIBUTORS AND FUNDING SOURCES

Contributors

This work was supported by a thesis committee consisting of Dr. Sarah Wolff [Chair] and Dr. Shiren Wand [Co-Chair] of the Department of Industrial and systems Engineering and Dr. James Paramore [Member] of the Department of Material Science and Engineering.

The data analyzed for this research was provided by Dr. Sarah Wolff and were presented in Solid Freeform Fabrication Symposium held in August 2021.

All other work conducted for the thesis was completed by the student independently.

Funding Sources

No other outside source of funding was provided.

NOMENCLATURE

AM	Additive Manufacturing
DED	Directed Energy Deposition
PBF	Powder Bed Fusion
FDM	Fused Deposition Modelling
CAD	Computer Aided Designing
STL	Standard Tessellation Language
3D	Three-Dimensional
2D	Two-Dimensional
SLS	Selective Laser Sintering
L-DED	Laser-Directed Energy Deposition
A-DED	Plasma Arc-Directed Energy Deposition
E-DED	Electron Beam-Directed Energy Deposition
IR	Infrared
X-ray	X-Radiation
CtFd	Computational thermo-Fluid Dynamics
Ti 6-Al 4-V	Titanium 6-Aluminum 4-Vanadium
SOM	Self Organising Maps
In718	Inconel 718 Alloy
APS	Advanced Photon Source
keV	kilo electron volt

TABLE OF CONTENTS

Page

LIST OF FIGURES

FIGURE Page

LIST OF TABLES

TABLE Page

1. INTRODUCTION AND LITERATURE REVIEW

1.1 Additive Manufacturing

The technological achievements in the field of electronics and computer science in the 20th century laid a foundation for a new age of prosperity and innovation. Today, information is produced and shared every second, purchases are made within the warmth of our homes and more time is spent towards being affluent as compared to surviving. Riding this mechatronic and computational wave, additive manufacturing (AM) has a become a part of many lives. Major automakers ,such as BMW, Lamborghini, Bugatti etc, use AM to make customised ornaments for their luxurious offerings, while, silicon valley startups such as Divergent are using 3D printing to challenge the Ford production line by mass customising cars. AM of rocket engines, combustors and reusable launchpads are core competencies of most startups in the space industry. Medical applications of AM are numerous, ranging from orthopaedic implants [2], tissue manufacturing [3, 4], drug delivery systems [5] and food fabrication [6]. It is a fact that Additive Manufacturing will play a key role in our future.

As opposed to a subtractive manufacturing process, additive manufacturing (AM) aims to build each part layer-by-layer. Based on the material used, AM can be broadly classified into metallic, ceramic and polymer, each material class has its own AM method and some methods being common. Based on process, AM can be categorised as, material extrusion (eg: Wire extrusion, fused deposition modelling (FDM) etc), material jetting [7]. binder jetting, laminated object manufacturing [8], direct energy deposition (DED) and powder bed fusion (PBF).

The complete process of AM starts similar to other modern manufacturing processes with a 3D CAD design followed by the analysis and optimisation of the design. After finalising the design it is converted to a .STL (Standard Tessellation Language) format file. A STL format represents the solid CAD part as a collection of triangular surfaces. In a STL file, the coordinates of each point of the triangles are mentioned along with the normal vector of the triangle [9]. This STL

file is pre-processed in a slicing software, which, slices the 3D geometry into 2D layers. After creating the slices for each layer, the file is converted into a g-code script which commands the tool head of the 3D printer to move and trace the path for each layer. Once the script is uploaded onto the system, 3D printing begins. The output of a 3D printer is in most instances not the final part. After 3D printing, the part is post-processed to ensure that the mechanical, metallurgical and surface quality standards are met. Post-processing can have more than one steps depending on the final part finish required. Support structures have to be removed for most AM builds in addition to the common post-processing done on machined or cast parts,such as, heat treatment, curing for polymers, coating etc.

Depending on the process and material selection, additive manufacturing requires the appropriate type of feed-stock material. FDM (Fused Deposition Modelling) uses either a granular or a filament based feed-stock material, PBF (Powder Bed Fusion), SLS (Selective Laser Sintering) and binder jetting techniques require a powder feed-stock.[10, 11]. DED (Directed Energy Deposition) can be used with either a powder feed-stock or filament feedstock.

In metal AM, PBF has been used industrially to a much larger extent than DED however, DED provides a greater opportunity to develop larger part sizes than PBF, functionally gradient parts, single crystal parts, high entropy alloys, repair work for broken parts, etc. A DED nozzle can be attached to a robotic arm of any size, which increases the dimensional flexibility of the process. Relativity space has used DED to create rocket engines by attaching a nozzle onto a robotic arm.

Directed Energy Deposition as the name suggests, deposits a layer of material by either melting it using a directed energy source or a kinetic energy source. This energy source can be a Laser (L-DED), Electron Beam (E-DED) or a Plasma Arc (A-DED). L-DED machines are manufactured by BEAM while Arcam and Sciaky sell the E-DED machines. DED is based on the basics of welding each powder layer on top of the other. Thus, we observe a cyclic heating and cooling process which refines the grains on previous layers as new layers are stacked. Laser based powder bed fusion is similar to laser welding, where keyhole instability contributes to porosity. Due to its stochastic nature as compared to powder bed fusion, laser based directed energy deposition has seen a great

interest in the field of material science and fluid mechanics.

Laser powered DED with powdered feed-stock leads to complex melt pool dynamics. Powder penetration into the melt pool and the carrier gas flow focused on the melt pool create an avenue for bubble formation which is not seen in the PBF method. Additionally, the interference in laser beam due to flowing powders cause higher fluctuation in the melt pool [12]. Thus, there is greater interest in the melt pool dynamics of laser powered DED with powdered feed-stock.

Infrared thermal imaging is a promising method for process monitoring of metal directed energy deposition [13]. Infrared radiation emitted from the surface of the melt pool has is detected by Infrared pyrometer, which converts the radiation into electric signals [14]. The infrared radiation emitted by a true black body can be used to give us the actual temperature of the black body. However, for metallic objects, the infrared emissivity is very low [15, 16]. Thus, in order to measure the melt pool surface temperature accurately, the infrared emissivity of the surface needs to be found. Chapter 3 of this thesis applies the calibration factor used by B Gould et al. [17] to calculate the infrared emissivity of the melt pool dynamically. Lastly, the shortcomings of the current method are discussed which lead to the avenue for future work in this field

1.1.1 Porosity

As in any other manufacturing process, AM has its own unique challenges such as surface finish, surface hardness, residual stresses [18], removal of support structures, high product lead time and porosity. Porosity is known to drastically reduce the static and fatigue loading capacity of components [19, 20]. However, it is seen that there is a critical diameter of porosity above which a significant decay of mechanical properties is seen [21]. This critical diameter depends on the material choice. Shaocheng Ji et al. [22] derived an analytical formula to show that the mechanical properties of a porous material depend on the size, shape, distribution and orientation of the pores with respect to the direction of loading. Porosity was found to cause directional heterogeneity in strain [23]. Controlled porosity can be induced in parts to control its direction of heat conduction or reduce its conductive abilities. As shown in the case of ceramics, porosity has a negative influence on heat conductivity [24], thus calculated porosity will allow us to add heat conductivity gradient

into the final printed part as well.

In-situ high speed X-ray imaging on L-PBF (Laser-Powder Bed Fusion), has shown that critical instability of the keyhole leads to the commonly known phenomenon of keyhole porosity [25]. Bobel et al. [26], showed that the keyhole porosity is formed from an unstable back wall of the keyhole. Martin et al. [27] delved deeper into the mechanics of pore formation from the back wall of the keyhole. Zhao et al. [28] also classified two mechanisms of pore formation from the keyhole, critical instability and acoustic. As the process of DED is similar to that of laser welding, which is a more mature field of research, Matsunawa et al. [29] showed that an optimal laser power is required to prevent the keyhole instability. They also recommended a pulsed laser input to prevent the keyhole from instability. However, this pulsed laser input needs to be carefully monitored as it can also induce keyhole porosity due to rapid closing of the keyhole depression [30]. Additionally, use of solid soluble shielding gas helped reduce keyhole porosity formation in their research. In DED, porosity can be caused by process parameters such as laser power density [31, 32, 28], laser focal point position, powder focal point position [11] and the track layout [33]. Porosity can also be brought into the part due to low quality powder feed-stock [34] and the penetration of the carrier gas into the hot melt pool [12]. Powders used in additive manufacturing are usually gas atomized. Thus, some powders have porous inclusions formed during the atomisation process. Incomplete break-up of droplets and release of dissolved gases during droplet solidification are postulated to be major causes of intra-powder porosity [35]. It is a well know fact that certain gases are soluble in molten metals but as the temperature decreases, its solubility decreases and these dissolved gases are released inside the partially solidified melt pool forming spherical bubbles [36]. Due to rapid solidification, most of these bubbles do not make it to the surface and solidify as pores.

Pore elimination through the absorption of bubbles into the laser keyhole has been proposed by Hojjatzadeh et al. [37]. This absorption is proposed to be due to a combination of the thermo-capillary force induced in the melt pool due to the thermal gradient and the drag force induced by the melt pool on the bubble. Lack of fusion pores are formed in interstitial gaps between partially solidified powders or due to rapid laser power reduction at the end of a track [31].

The various mechanisms for pore formation and their dependence on the in-situ process parameters can allow us to create functionally graded parts to optimise part weight and loading properties. This research points out a very commonly observed mechanism of pore size and distribution evolution, i.e coalescence. It looks at the influence of the location of bubble formation and transport on its ability to coalesce and form pores. This research is only one step in the direction of manipulation of melt pool bubbles to design pores into the final parts.

1.1.2 In-situ Infrared Thermal Imaging

As AM becomes mainstream, there is more focus on the optimisation of its processes. Intensive research has been done on the in-situ monitoring of the process using a plethora of sensors [38]. Pyrometers and IR-Cameras are used to gather thermal readings as thermal history of a part has a strong correlation with the microstructure and cracking of the final part. Additionally, cameras that detect visible signals are used to determine track dimensions and surface defects [38]. Mazumder et al. [39] have used spectral data from the gas plume, which is formed out of the vaporised substrate, to estimate the material composition of the part in-situ. One of the most recent methods to study the melt pool is using high speed in-situ X-ray imaging to analyse the melt pool flow under the surface. Wolff et al. used the in-situ X-ray monitoring to observe the melt pool flow dynamics and porosity formation during DED [1]. As it is difficult and expensive to continuously monitor the characteristics of the melt pool in-situ, Wolff et al. [40] developed a CtFD (computational thermo-fluid dynamics) model to analyse the laser cladding of In718 on carbon steel. It is seen that the input laser power is attenuated by the powder flowing above the melt pool. The magnitude of this attenuation is directly co-related with the powder flow rate and the laser power.

Machine learning has been used to efficiently and accurately predict porosity real time prediction of porosity. Khanzadeh et al. [41] used Self-Organizing Maps (SOMs) to predict the location of porosity using in-situ surface thermal sensing.

In-situ thermal imaging is vastly used in the metal AM industry. It is well known that the thermal history of a 3D printed part greatly influences its final quality. In-situ process control is an essential part of any metal 3D printing machine, however, it is very important for directed

energy deposition due to its stochastic nature. In-situ sensing has been used to train AI models to draw out correlations between the process parameters and final part quality [42]. However, one of the greatest hurdles for accurate measurement of the surface temperature using its infrared (IR) radiation is the constant fluctuation of its surface IR emissivity. B Gould et al. [17] used a calibration factor to estimate the true surface temperature of the melt pool for L-PBF of Ti 6-Al 4-V powders. They use the radiometric temperature at the boundary of the melt pool to extrapolate the temperatures at other points in the melt pool. As the authors mentioned, this method is not very accurate to define the temperature at hotter regions of the melt pool as the emissivity changes with temperature and surface roughness but it does provide an idea of the variation of emissivity with respect to time. This research uses this technique on the laser powered directed energy deposition of Ti 6-Al 4-V and molybdenum to visualise this change in emissivity with time.

2. PORE COALESCENCE IN LASER BASED DIRECTED ENERGY DEPOSITION*

2.1 Motivation

The formation mechanisms of porosity are well studied for PBF. Stability of the keyhole is one of the most important factors to prevent porosity. Re-melting of the surface has been shown to reduce surface roughness, however, definitive research on its ability to eliminate porosity is not available [23, 43]. During surface re-melting, bubble coalescence leads to larger pores in reduced quantity. As coalescence depends on the bubble collision in the liquid [44], which should be facilitated by bubble density in a liquid, surface re-melting should eliminate pores after they have coalesced because of their fewer quantity and larger size. In subsequently printed layers, pores formed during previous layers are seen to evolve in the experiments conducted by Wolff et al. [1]. This evolution comprises of morphological changes such as size and shape of individual bubbles as well as coalescence of multiple bubbles.

Due to the micro-scale of the porosity formed underneath the melt pool surface and the small time scales in which bubbles transform their shape and size before solidifying, evolution of bubbles is not well understood. Preventive measures to avoid porosity have been discussed above, but without a deeper understanding of the life of a bubble after it is formed, we cannot create novel methods to eliminate porosity after they are formed. Understanding the mechanics of bubble evolution after they are form can provide an opportunity for the accurate location of pores and their size distribution. Input parameters can be controlled during the process to assist or retard morphological changes in the bubbles.

Changes in the size and shape of bubbles are an important field of study to predict final part porosity. They depend largely on the flow field around the bubbles which is governed by input variables such as laser parameters, powder flow and carrier gas flow into the melt pool. While, studying the bubble evolution in DED is a substantial problem, coalescence of bubbles is the only

*Reprinted with permission from "In-situ Observations of Directed Energy Deposition Additive Manufacturing Using High-Speed X-ray Imaging" by Sarah J. Wolff et al, 2020. JOM Journal of the Minerals, Metals and Materials Society, Vol. 73, 192, Copyright [2021] by Texas A&M University.

evolution that takes place due to the interaction of one bubble with another. Due to this added complexity, coalescence is studied in this research, while, future research will create a complete understanding of all morphological changes experienced by bubbles in the melt pool. It is expected that coalescence should reduce the quantity of bubbles present in the melt pool while creating larger bubbles which are easier to locate and destroy. This opens up an opportunity for post processing layers to reduce porosity tactically. Thus, this study uses known contributors of coalescence such as frequency of bubble contact and time of bubble contact to point out significant factors that lead to coalescence.

2.2 Past Work*

The data used in this experiment was collected by Wolff et al. [1]. They used the 32 ID-B beamline at the Advanced Photon Source (APS) at the Argonne National Laboratory. This beam line was developed at the APS to accommodate high speed X-ray imaging in monochromatic and white-beam modes [45]. A white X-ray beam was used at 24 keV energy for its first harmonic . A single-crystal scintillator converted the X-rays into visible light. This scintillator was 100 μm thick and 10 mm in diameter. The visible light was magnified by a 5X microscopic lens followed by a tube lens and collected by the Photron SA-Z high-speed camera. The images were 896 by 776 pixels with exposure time 10 μs and collected at a frame rate of 30000 frames per second.

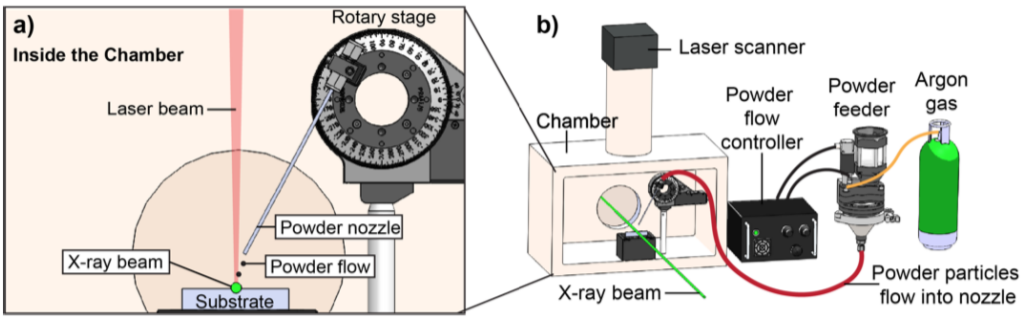

Figure 2.1: (a) A close-up of the set-up (b) The set-up with the X-ray, Reprinted with permission from [1]

For the experiments used in this research, a 540 W continuous-wave Ytterbium laser was used at a scan speed of 100 $\mu m/s$ with a beam diameter of 100 μm and a $D4\sigma$ Gaussian profile. It was operated at 216 W. The total scan distance was 1.4 mm on a 30 $mm \times 10\ mm \times 406\ \mu m$ Ti 6-Al 4-V substrate. Argon shielding gas was used at intervals of 100 μs through a 200 μm steel nozzle at 172 kPa. Plasma atomized Ti 6-Al 4-V powder with sizes between 45 μm and 106 μm using a Gaussian distribution were mixed with irregular Ti 6-Al 4-V powders. This mixture was delivered from a hopper using a remotely controlled rotary servo motor rotating at 1 rpm with a pulse width of 400 ms. A galvanometer laser scanner was used to control the laser beam hitting the substrate. The infrared camera was positioned such that its horizontal angle with respect to the X-ray beam was 25°.

The X-ray images provided by the researchers at Argonne have a resolution of 1.95 μm per pixel, whereas, the IR images have a resolution of 30 μm per pixel. The frame rate of X-ray images and IR images are 30000 fps and 10000 fps respectively. The axis of the IR camera was at an angle of 20° to that of the X-ray beam. Table 2.1 gives a list of other experimental parameters. The substrate material was the same for all the experiments, however, the powders for the first two experiments were a mixture between spherical and irregular powders. Whereas, the 3^{rd} and 4^{th} experiment consist of only spherical powders. As this analysis was on the coalescence of bubbles after they are formed, the experiments with spherical powders reduce the number of bubbles formed in the experiment. Disc speed of the powder hoppers controlled its powder flow rate and were set at 1 rpm for all the experiments. The powder flow rate observed during the first laser pass was lower in exp. 1 as compared to exp. 2. The powder flow rate was comparable during the second pass. Exp. 3 has a low powder flow rate during the entire experiment whereas, exp. 4 has a higher powder flow rate as compared to exp. 3. The angle between the powder nozzle and the vertical was 45°. The deposition delay, as shown in Table 2.1, indicates the time lag between switching ON the powder hopper and the laser. Experiments with Molybdenum require a higher heat input to melt the powders and hence, the laser power used was higher. The Gas and Wheel pulse stand for the time interval for which the respective equipment was turned ON. An appropriate interval

was required for longer life of the equipment and reduced time spent maintaining the equipment. Each experiment had two tracks where the second track partially overlapped the first track while tracing its path in the opposite direction. The IR filter provided a high radiation temperature range of 537 $^{\circ}C$ to 1567 $^{\circ}C$. The X-ray images are 16-bit and 896 px$\times$776 px in dimensions.

Table 2.1: Experimental parameters for the experiments conducted by [1]

Parameter Name	**Exp. 1**	**Exp. 2**	**Exp. 3**	**Exp. 4**
Substrate Material	Ti 6-Al 4-V	Ti 6-Al 4-V	Ti 6-Al 4-V	Ti 6-Al 4-V
Powder Material	Ti 6-Al 4-V	Ti 6-Al 4-V	Molybdenum	Molybdenum
Powder Shape	Irregular & Sph.	Irregular & Sph.	Spherical	Spherical
Disc Speed (rpm)	1	1	1	1
Gas Pressure (PSI)	25	25	25	25
Nozzle Angle ($^{\circ}$)	45	45	45	45
Deposition Delay (s)	0.79	0.79	0.9	0.9
Gas Pulse (ms)	400	400	400	1000
Wheel Pulse (ms)	20	20	0.1	0.1
Laser Power ($\%$)	40	40	60	60
Scan Speed (ms^{-1})	0.1	0.1	0.1	0.1
Scan Distance (mm)	1.4	1.4	1.5	1.5
IR Filter Temp. Range (K)	537 - 1567	537 - 1567	537 - 1567	537 - 1567
Powder Flow Rate	First pass - Low	First pass - High	Low	High

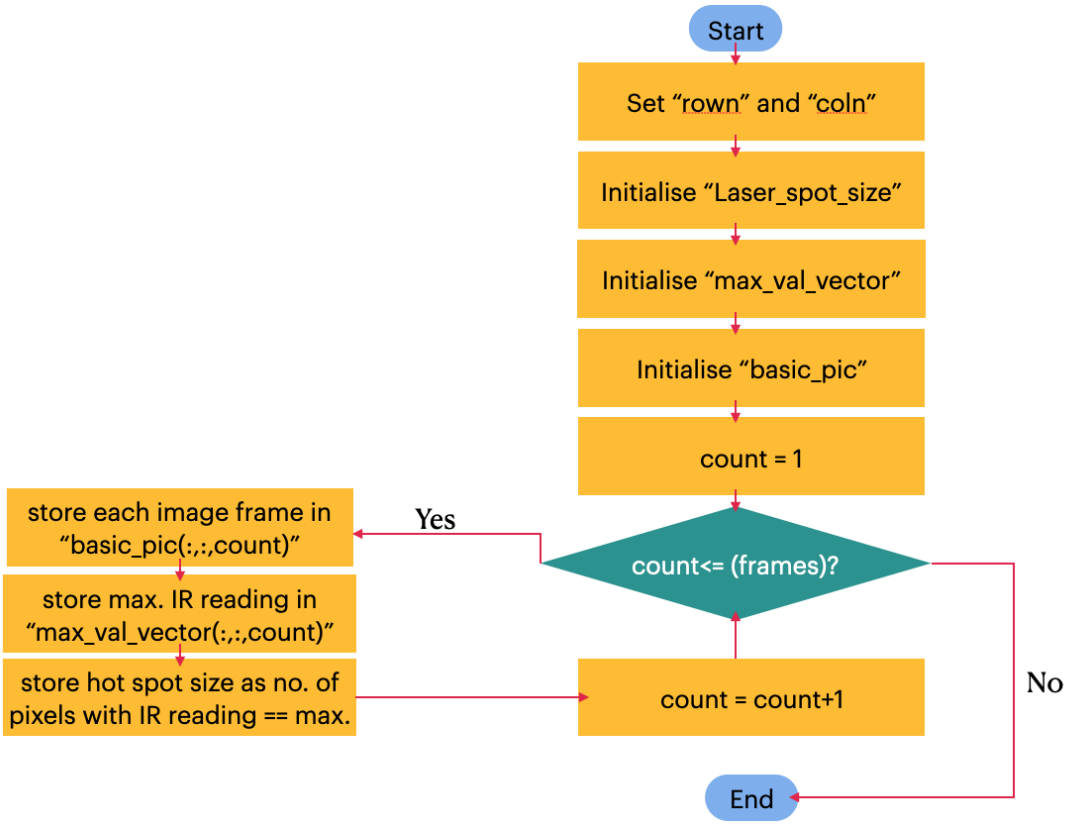

Figure 2.2: Flowchart of initialising the IR images into an array

2.3 Mechanics of Bubble Coalescence

Bubble coalescence is a well understood phenomena in fluid mechanics. As a thumb rule, coalescence is dictated by the frequency of contact between parent bubbles and the efficiency of the coalescence process [44]. Using a probabilistic theory, the probability of coalescence can be found by multiplying the probability of bubbles being in contact with the efficiency of coalescence [46]. The bubble approach velocity and the viscosity of the liquid medium have been shown to influence the coalescence process of bubbles [47].

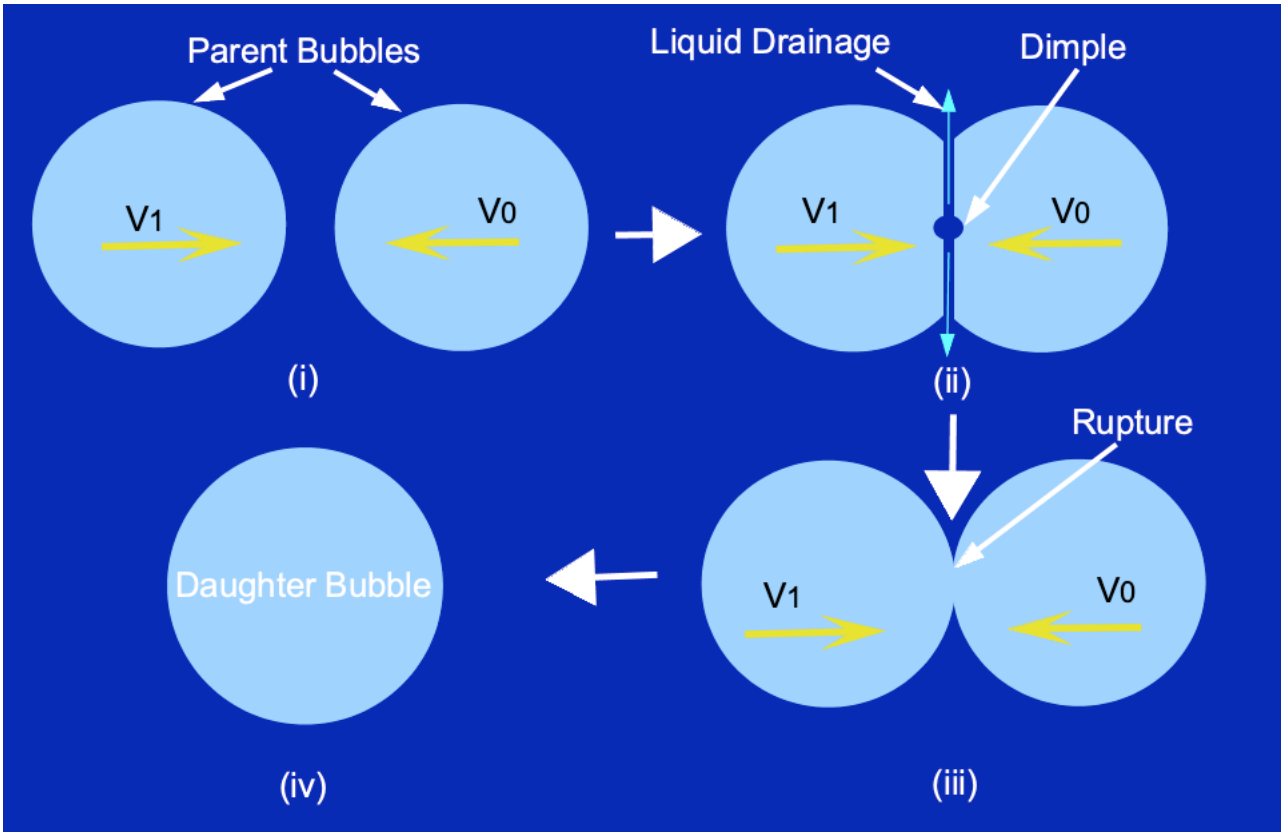

Figure 2.3: Mechanics of bubble coalescence, (i) Parent bubbles approach each other, (ii) they come in contact and the liquid film trapped in between starts draining out, (iii) the film surface between them ruptures and they coalesce, (iv) the daughter bubble is larger in diameter than each bubble but smaller than the sum of diameters of the parent bubbles

Bubble coalescence requires two phenomenon to occur in succession, the bubbles should come in contact with each other and the bubbles that come in contact should coalesce. According to the review on the mechanics of bubble coalescence by Liao et al. [44], the drag force created on the bubble by liquid surrounding the bubble push the bubbles towards or away from each other. A differing buoyancy between bubbles is an exception to the drag induced collision between bubbles. The authors reviewed the most widely used models to quantify the probability of coalescence after the bubbles contact each other. These models comprise of an energy model where the kinetic energy of the bubbles colliding should exceed the surface energy of these parent bubbles, a velocity model that suggests an optimal approach velocity and a film drainage model which is based on

the contact time between parent bubbles. The film drainage model takes into consideration the mechanics of coalescence, i.e, as compared to the other models it rigorously looks at the bubbles coming in contact to drain out the liquid film in between these bubbles. After drainage, the surfaces of both bubbles rupture to coalesce into one single bubble.

The localized liquid flow surrounding two or more bubbles dictates their chances of coalescence. In a complex flow with a stochastic energy input, into the melt pool leads to multiple flow inducing forces. Marangoni convection due to a thermal gradient on the surface of the melt pool leads the liquid away from the hot laser spot towards cooler regions [48]. This induces a flow inside the melt pool where cooler liquid particles present deeper in the melt pool are driven towards the hot region on the surface. In addition to this convection, which is more dominant force in L-PBF, the powder particles entering a melt pool create localized pressure gradient across the particle, such as, in the wake of the particle. The quantity of bubbles present in the melt pool during each time step of 0.1 ms provides an understanding of the increment in bubble density inside the melt pool. At the same track distance covered by the laser, a higher quantity of bubbles signifies a higher bubbles density. This higher bubble density increases the chance of bubbles coming in contact and hence, coalescence.

After the bubbles come in contact with each other, they may or may not coalesce. Coalescence between two bubbles in contact occurs under the influence of two competing forces, i.e., Van der Waal's forces that initiate the rupture of bubble surface leading to coalescence and the increase in free energy of the system due to the deformation of bubbles [49]. A film drainage model as shown by Liao et al. [44] considers the time taken for bubbles to move closer to each other and coalesce. This time is called as the drainage time between the bubbles, as this is the time required for the liquid film present in between the bubbles to drain out and allow the bubble surfaces to rupture in order to coalesce. The real time that a pair of bubbles are in contact is known as the contact time. For bubbles that approach each other and coalesce, the contact time is equal to the drainage time. This drainage time depends on the characteristics of the bubbles under consideration and the external force applied onto the bubble bringing them together [50]. As compared to the energy

model and critical velocity models, the film drainage model is derived based on the mechanics involved in coalescence.

2.4 Mechanics of Bubble Coalescence in Directed Energy Deposition

No published literature has discussed the mechanics of coalescence in DED yet. The melt pool flow during directed energy deposition of powders is a complex phenomenon. The local flow can change rapidly due to the penetration of a new powder as well as the melting of previously deposited powders. To simplify the analysis of coalescence, without introducing the complexity associated with a localized flow analysis, broader factors that influence the melt pool flow are taken into account. These broader factors include the relative position of the laser from the points of coalescence, the fluctuation in keyhole depth and the quantity of bubbles formed in each time step of 0.1 ms. These factors are used to search for a causal relationship between occurrences such as powder penetration, layer number, powder shape, laser power attenuation and melt flow due to the laser energy. The local melt flow governed by laser input energy would be dependant on the position of coalescence relative to the laser input. To categorize this further, the position of coalescence was divided into those that occurred preceding the keyhole and those that occurred in its wake. This categorization was done as the melt flow preceding the keyhole is governed by hotter fluid with minimal are available for the penetration of powder into the melt pool without fusion. Thus, bubbles formed preceding the keyhole were only due to the fusion of partially fused surfaces. These bubbles had a shorter lifetime and hence, it would be expected that coalescence is rather improbable and requires a calmer melt flow. However, coalescence was observed and the coalesced bubbles were engulfed by the keyhole. The melt flow following the keyhole had more space for the powders to penetrate the melt pool, had cooler temperatures and allowed the bubbles to settle at the bottom of the melt pool before interacting with one another. This was driven by the belief that bubble coalescence should be dominant in the wake of the keyhole. Additionally, the phenomenon of coalescence has no physical significance if it does not affect final part porosity. Thus, it is necessary to see if the porosity preceding the keyhole adds to final part porosity.

The keyhole depth is another major factor that can point out to specific irregularities in the

melt pool flow that leads to coalescence. The keyhole is formed due to the back pressure generated by vaporization of metal by the laser. The instability of keyhole is known to result in keyhole porosity, that is observed in laser welding and powder bed fusion. This keyhole porosity is formed when the opening closes up without allowing the gas generated at its bottom tip to escape. Thus, a high fluctuation in keyhole depth should show a higher porosity, leading to a higher probability for coalescence. Furthermore, the keyhole depth is also an indication of the conversion of laser energy to metal vapor. Thus, if the same laser spot power creates differing keyhole depths in different locations for the same material then the region with a lower keyhole depth has used the laser energy to fuse more material. While it is possible that the laser power may have been attenuated by powder interference, such a reduction should be for a few frames. Thus, the fluctuation in the keyhole depth is studied to quantify the keyhole instability with a hypothesis that keyhole fluctuates with a higher frequency where more bubbles are formed.

2.5 Methodology

The experiments considered for this study were selected based on the bubbles created in these experiments. To study coalescence an abundance of bubbles need to be present in the melt pool. To study the influence of powder interaction with the melt pool flow, Exp. 1 and 2 were compared to Exp. 3 and 4. Ti 6-Al 4-V powders fused into the substrate with input laser power, whereas, Molybdenum powders did not. Additionally, the irregular nature of powders in Exp. 1 and 2 were expected to have a higher porosity in their parts because of the introduction of surrounding gas in the wake of irregular powders entering the melt pool. Fig. 2.4 shows the X-ray images as received from Dr. Wolff [1].

The X-Ray images for experiments were downloaded from Dr. Wolff's Box drive. Each folder consisted of images for one entire experiment. These folder were then dragged onto the toolbar for FIJI to open them up as a stack. Once these stacks were loaded, the Analyse $\rightarrow$ Set Scale option was used to set each pixel as 1.95 μm. The Image $\rightarrow$ Adjust $\rightarrow$ Brightness/Contrast option was used to adjust the brightness and contrast of the entire stack for clearly visualising the keyhole and bubbles. The brightness and contrast settings were visually adjusted for each experiment based on

the visibility of keyhole and bubbles. Further adjustments were made to the brightness and contrast to view the fusion of powders settled on the substrate.

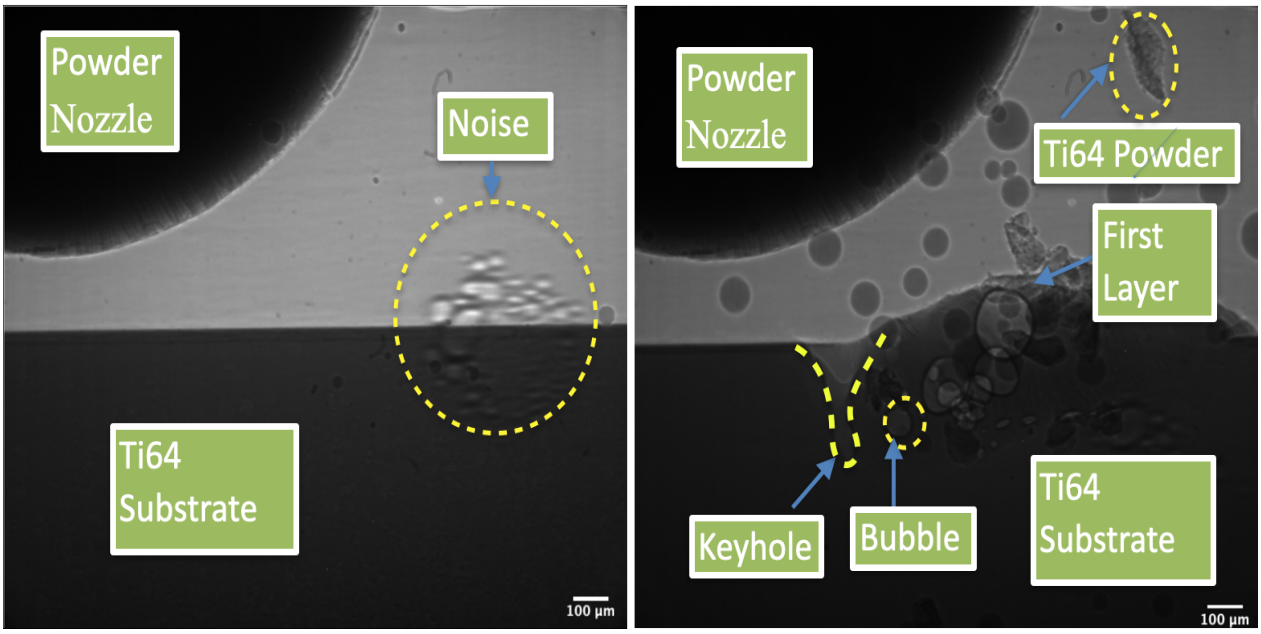

(a) Background X-ray image

(b) Sample X-ray image

Figure 2.4: Raw X-ray images taken from Exp. 1, which used Ti 6-Al 4-V powders on a Ti 6-Al 4-V substrate with a spatial resolution of 1.95 μm

As mentioned earlier, three studies were performed to understand the surrounding conditions that led to bubble clusters being formed.

2.5.1 Location of Coalescence with respect to the Keyhole

As stated in Section 2.3, the location of coalescence with reference to the keyhole is important because it gives us a reference to understand certain characteristics of the melt pool flow because the laser energy is a major driving force for the melt pool. This was categorized into two areas, that are, preceding the keyhole and in the wake of keyhole (Fig. 2.5). As shown in Fig. 2.4b, the keyhole can easily be distinguished during the process.

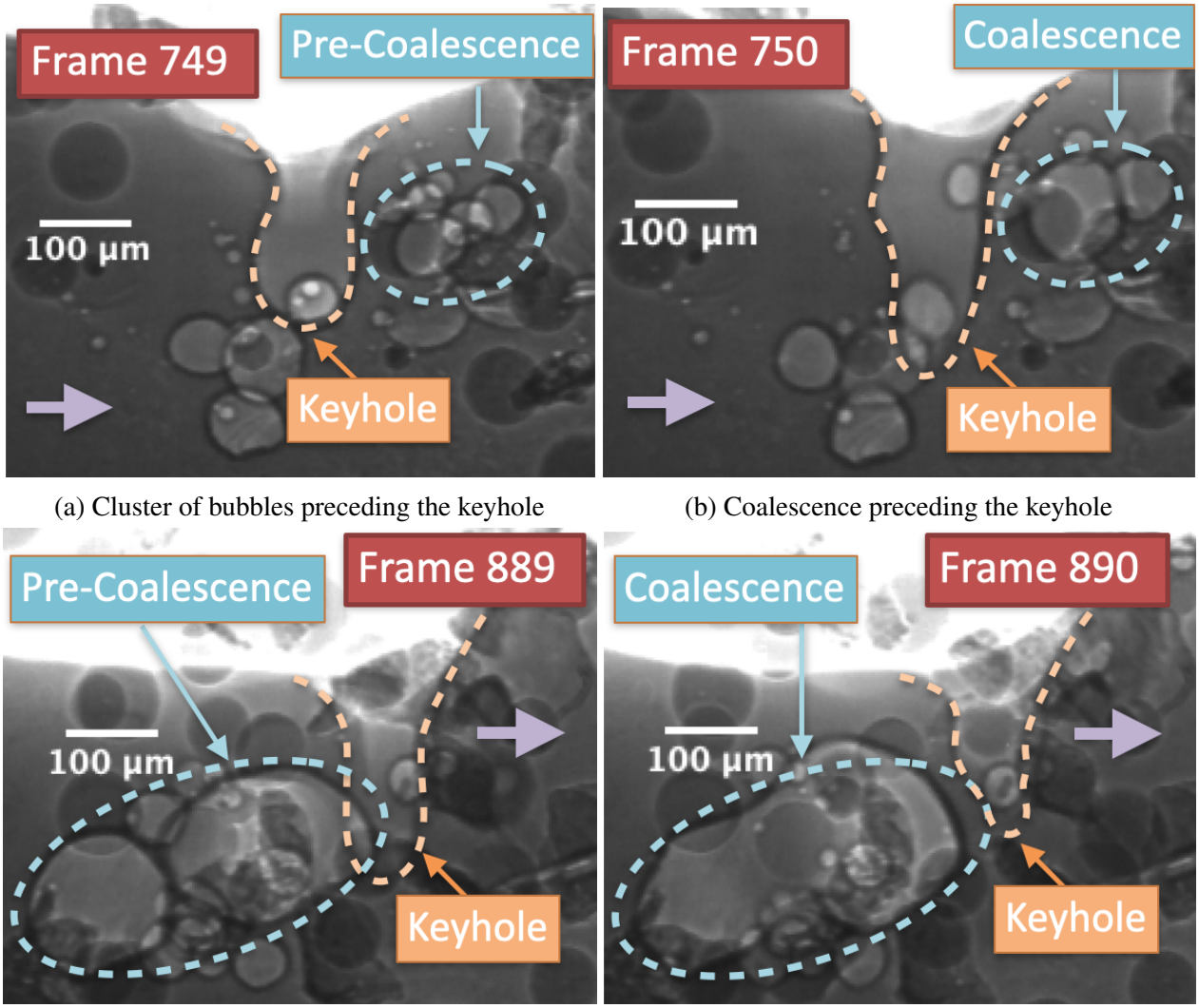

(a) Cluster of bubbles preceding the keyhole

(b) Coalescence preceding the keyhole

(c) Cluster of bubbles in wake of the keyhole

(d) Coalescence in wake of the keyhole

Figure 2.5: Coalescence that occurs preceding and in wake of the keyhole (Images are taken from the second laser pass of Exp. 1 and the purple arrow shows direction of laser travel)

Coalescence is considered to occur when neighboring bubbles come in contact with each other and are replaced by a bubble larger than either bubble in the next frame. There is a change in shape of the bubble, which indicates the joining of two spherical entities or the two bubbles can't be seen anywhere else in their neighborhood. To confirm coalescence, the bubbles are tracked for a few frames preceding coalescence to extrapolate the expected position of each bubble at the frame of coalescence if coalescence hadn't occurred. In a dense cluster of bubble with fluctuating sizes and

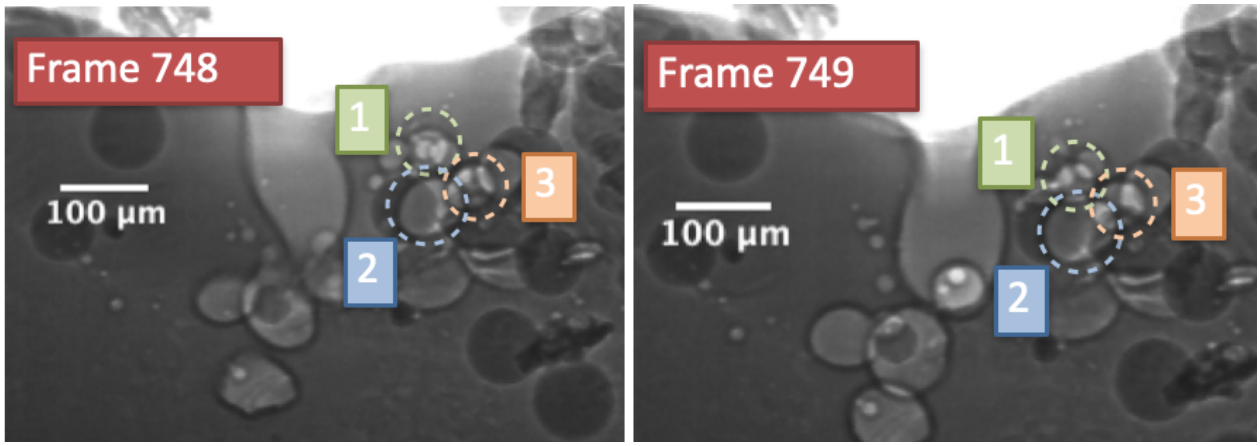

(a) Bubbles 1 and 3 are in contact with Bubble 2

(b) Bubbles 1 and 3 come closer to Bubble 2

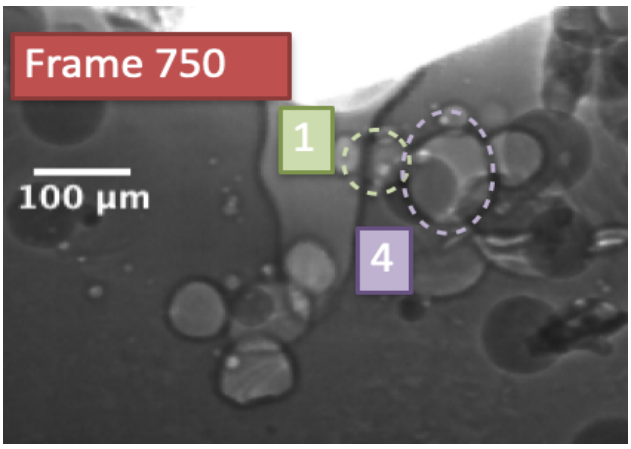

(c) Bubble 3 coalesces with Bubble 2 and the resulting Bubble 4 pushes Bubble 1 away

Figure 2.6: (a) and (b) show three bubbles that are considered during coalescence (c). It is concluded that bubbles numbered 2 and 3 coalesce as they cannot be seen in (c) and a deformed and larger bubble replaces them. Whereas, Bubble no. 1 has been displaced from its original position.(Exp. 1 which uses Ti 6-Al 4-V powders is used for this example)

shapes, care had to be taken to distinguish between, coalescence and the concurrent increase in a bubble's diameter accompanied by a sharp decrease in its neighboring bubble's diameter. Many bubbles changed their position during the frame of coalescence drastically and the extrapolation helped to detect whether the bubble had changed its position instead of coalescing. Fig. 2.6 shows an instance where a bulge in the daughter bubble (Fig. 2.6c) is directed towards the position occupied by Bubble no. 1, however, Bubble no. 1 has moved its position drastically towards the left. Additionally, the coalescence phenomena could have been easily overlooked in a dense cluster

of bubbles. To avoid this error, steps of 3 frames are taken at a time and were analysed a minimum of 3 times but more repetitions were done when dense clusters were involved until all bubbles present in these frames were considered.

After the coalescence has occurred, the new bubble's evolution was tracked throughout the experiment to understand how they influenced the final part porosity. As opposed to coalescence, it was relatively easier to track the daughter bubble throughout its lifetime. A conclusion was drawn between the influence of the coalescence occurring preceding the melt pool and that occurring behind it.

2.5.2 Keyhole Depth

The keyhole depth for each time step (0.1 ms) was extracted manually using FIJI and its line feature, which can be used to measure distances between two points in each image. The resolution of each image was set using the "Set Scale" function in FIJI. In these images, 1 px translates to 1.95 μm.

The vertical distance between the lowest point of the keyhole and the keyhole opening where a sharp bend is seen was used as a measure for the keyhole depth. Measuring the keyhole depth is a straightforward task when measuring it for the first laser pass, as the flat substrate on its leading edge provides a stable reference (Fig. 2.7a). However, topmost point of the keyhole cannot be easily seen during the second laser pass. This is due to an uneven surface created after the first laser pass, as seen in Fig. 2.7b. A relatively sharper bend is seen on the trailing edge of the keyhole during the second laser pass. The point at which the sharpest bend is seen at the opening after which the keyhole opens up into the melt pool surface is used as the second reference point to measure the depth from.

This measurement of the keyhole depth is plotted in MATLAB, using a box plot and its distribution was compared between the first and second passes of the experiments as well as the difference in its distribution between the different experiments. Once the difference in its distribution is noted, a further detailed plot is created against time (ms). The time at which coalescence occurred was also marked on the same plots to observe the keyhole depth at these time steps. To

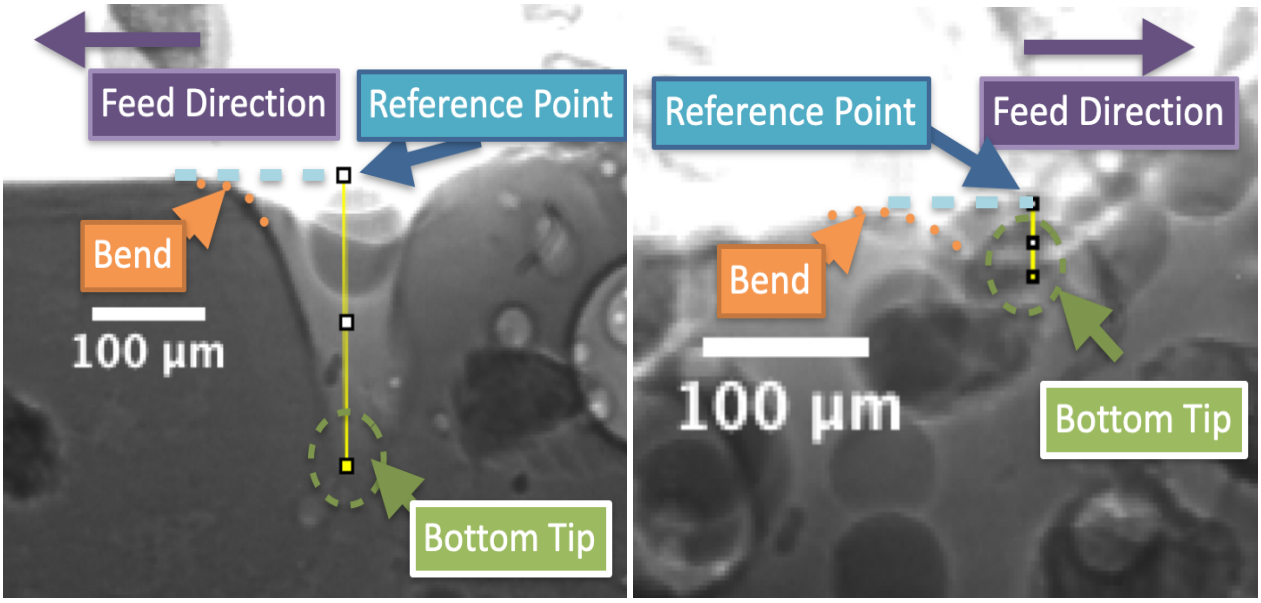

(a) First Laser Pass (b) Second Laser Pass

Figure 2.7: Measuring the Keyhole Depth using line tool in FIJI (Exp. 1, which was conducted using Ti 6-Al 4-V powders is displayed)

aid in future research work, where correlation between calibrated IR images and the keyhole depth will be drawn, the time used here was calibrated from the start of the IR image. This calibration was done by using the laser's starting frame as a reference frame. The time elapsed after it starts is noted down for X-ray images using the frame stamp in its window. This time was added onto the time at which the laser started in the IR images.

The plots were studied for important spikes and depressions. These time slots were studied back in the X-ray images to get the reason behind those changes.

2.5.3 Bubble Quantity

The quantity of bubbles present in the substrate in each time step (0.1 ms) was calculated manually. This calculation was done two times at the same time by counting from left to right followed by right to left. All visible bubbles were considered during the count. Additionally, counting was performed at specific frames of interest such as those that showed a huge spike in the quantity of bubbles present.

At the end of the first laser track, bubbles generated tended to solidify into pores. The pores created at the end of the first pass also contribute to the bubbles present in the melt pool as the laser marches on during the second pass. It can be said that the solidified pores formed at the beginning of the first laser track will not contribute towards the bubbles dynamics during the beginning of the second laser track, however, they are still considered as this allows for an instantaneous count of the total no. of pores present in the substrate at each time step as well. Additionally, the increase in bubble quantity could be observed as spikes in these plots. The time at which dominant spikes that were observed got looked at closely to point out the underlying cause.

MATLAB was be used as the application for data processing. Box plots were be created to show the distribution of the number of bubbles in each frame for the first track, second track, frames of coalescence and the entire experiment. The distribution of contact time of parent bubbles before coalescence was shown through box plots.

2.5.4 Bubble Size

Bubbles diameter was used to compare the bubble sizes for three categories of bubbles, Parent Bubbles, Daughter Bubbles and Final Porosity (see Fig. 2.6a). The Parent Bubbles are bubbles that coalesce to form a corresponding Daughter Bubble. Parent Bubble diameters were measured in the frame preceding their coalescence, whereas, Daughter Bubble diameters were measured on the frame of coalescence. The diameter of spherical and near spherical bubbles were calculated by using the "line tool" in FIJI. However, many bubbles had irregular shapes, especially larger bubbles formed after coalescence and some pores formed at the end of experiments. The effective diameter of these shapes was calculated by measuring the perimeter of the pore and dividing its value by π.

Fig. 2.8 shows the two methods used to extract the diameter of bubbles in the experiments.

2.5.5 Contact Time

Coalescence only occurred during Exp. 1 and 2, which used irregular and spherical Ti 6-Al 4-V powders. Thus, the contact time for coalescence was only calculated for these experiments. For the contact time to be calculated, the frame at which coalescence was observed was noted down and

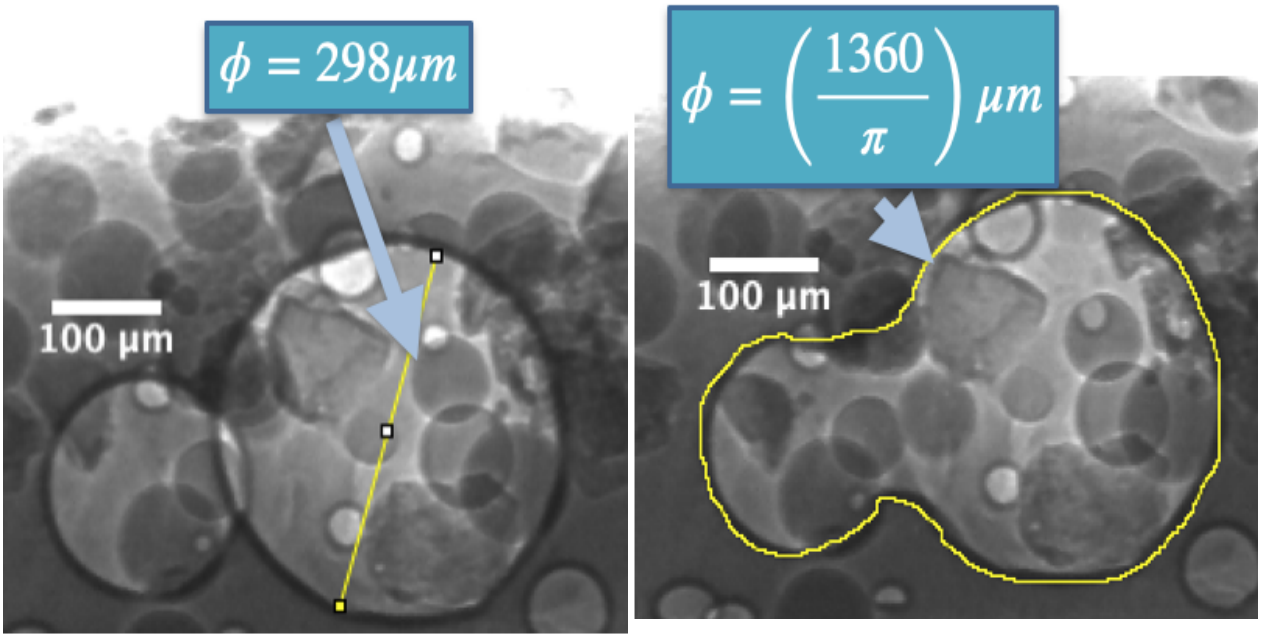

(a) Measuring the diameter of a near spherical bubble

(b) Measuring the diameter of an irregularly shaped bubble by dividing its perimeter by π

Figure 2.8: Measuring the diameters of bubbles. (a) A near spherical parent bubble that coalesces to form (b) an irregularly shaped bubble. (Exp.1 is used to show the procedure of diameter extraction using FIJI)

the frames were observed in reverse. The frame at which the parent bubbles come into contact was noted down and subtracted from the frame at which coalescence occurs. Bubbles were considered to be in contact with each other if there was no gap seen in between them. This understanding of contact between bubbles is restricted by resolution of the X-ray images which was 1.95 μm. Hence, bubbles within 1.95 μm were considered in contact. The contact time was displayed as box plots to show the distribution.

2.6 Results

2.6.1 Morphological Changes in Bubbles

The size of bubbles change between their birth and solidification. This may be due to changes in the surrounding liquid flow, pressure and temperature. Fig. 2.9 shows the different types of morphological changes observed in the the experiments. These changes are in 3 categories that are

not mutually exclusive. The categories are, size (Fig. 2.9a & 2.9b), shape (Fig. 2.9c & 2.9d) and coalescence (Fig. 2.9e & Fig. 2.9f).

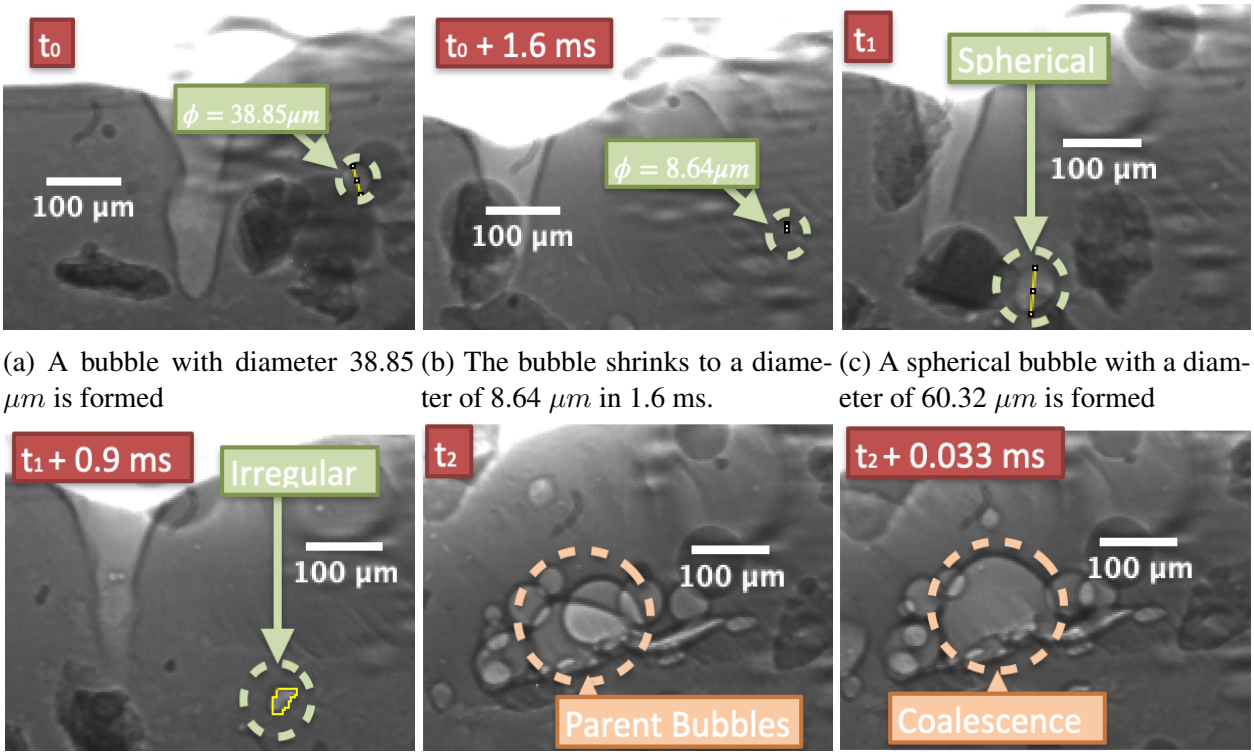

(a) A bubble with diameter 38.85 μm is formed

(b) The bubble shrinks to a diameter of 8.64 μm in 1.6 ms.

(c) A spherical bubble with a diameter of 60.32 μm is formed

(d) The bubble shape changes in 0.9 ms

(e) Two bubbles come in contact with each other

(f) The bubbles coalesce to form a larger bubble in 0.033 ms

Figure 2.9: Morphological changes undergone by bubbles after they are formed. (a) & (b) show the changes in bubble size, (c) & (d) show the changes in bubble shape, while, (e) & (f) show coalescence (Examples are taken from Exp. 1)

2.6.2 Position of the bubble coalescence relative to the keyhole

Figure 2.10 is a snippet of the laser beginning to trace a second track near a partially fused powders from the first track. In frame 702, the keyhole approaches a partially fused powder. As it got close (frame 703) enough to melt it, a cluster of bubbles were formed at the same point where the powder was in frame 702, the left most bubble in this cluster escapes into the keyhole, in frame 706, while the other two bubble remain in contact until frame 708 where they coalesce to form a

larger daughter bubble. As the keyhole marches on, in frame 715, the daughter bubble escapes into the keyhole. As a result, no bubbles generated earlier in the laser track actually cause porosity in the finished part. This situation is common for most of this laser path till the end. This is a very common result for bubbles formed leading the keyhole. Some exceptions occur at points where the keyhole depth is greatly diminished to absorb any bubbles formed in front of it or if the bubbles are very small and bypass the keyhole.

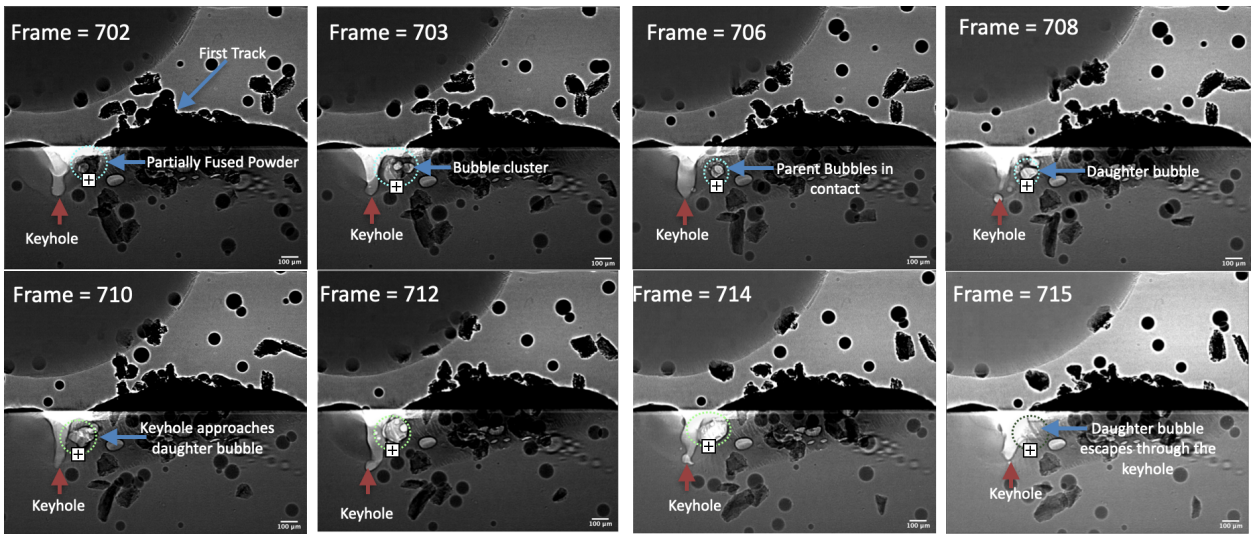

Figure 2.10: Bubble Coalescence in front of the keyhole and its escape into the keyhole during the second pass of the laser

To know more about the bubbles that form final porosity, we need to pay more attention to the bubbles formed in the second half of the track where most bubbles are formed in the wake of the melt pool. In fig. 2.11, the melt pool started to cool down on the surface reducing powder entry into the melt-pool. In frame 910, a cluster of bubbles were formed in the wake of the melt-pool, out of this, most bubbles burst either due to powder entering the melt pool, coalesced with neighboring bubbles or escaped from the surface. However, 3 bubbles coalesced and sunk into the melt-pool. They do not burst and provide an opportunity for other bubbles to coalesce. As the laser moves forward the perturbations on the bubble surface reduced and one pore larger that any new bubble

formed was remnant after two laser passes.

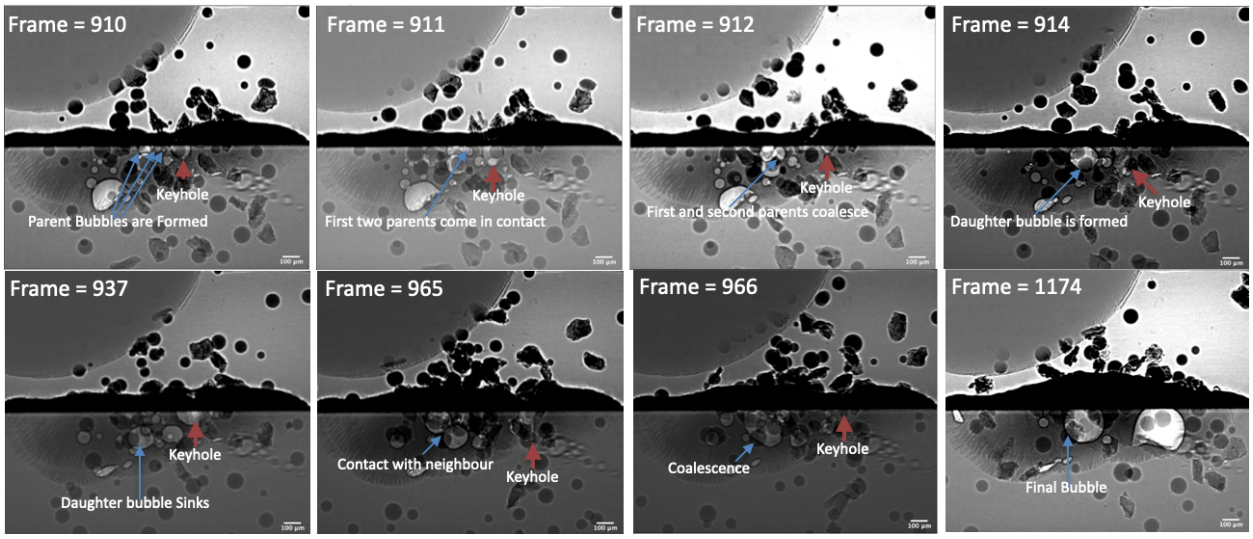

Figure 2.11: Frame 910 - 966, Bubble Coalescence after the keyhole during the second pass of the laser and frame 1174 shows the final porosity after both laser passes

Figure 2.11 shows that there were more bubbles in each frame in the second track which, as shown earlier, was due to the re-melting of partially fused powders and the presence of pores leftover from the first track. The quantity of bubbles present in the melt-pool that leads to coalescence has a large range, thus, its relationship between bubble density and pore coalescence is not straightforward as many highly dense bubble clusters do not result in bubble coalescence. Even as 45 instances of coalescence were observed in the second track which had more bubbles present in each frame as opposed to the first track.

2.6.3 Keyhole depth and Bubble quantity in the melt-pool

There is a stark difference between the fluctuation of the keyhole depths for Ti 6-Al 4-V experiments and Molybdenum powders experiments. In Fig. 2.12, experiments 1 and 2 show a dip in the keyhole depths observed during the second track. This dip occurs when the laser is in the middle of laying down the second track. This region is also where there is the highest quantity of partially fused Ti 6-Al 4-V powders. This reduction in the keyhole depth is not observed in

the Molybdenum experiments, however, there is a greater fluctuation in the keyhole depth for the second track. This observation is consistent with all the experiments.

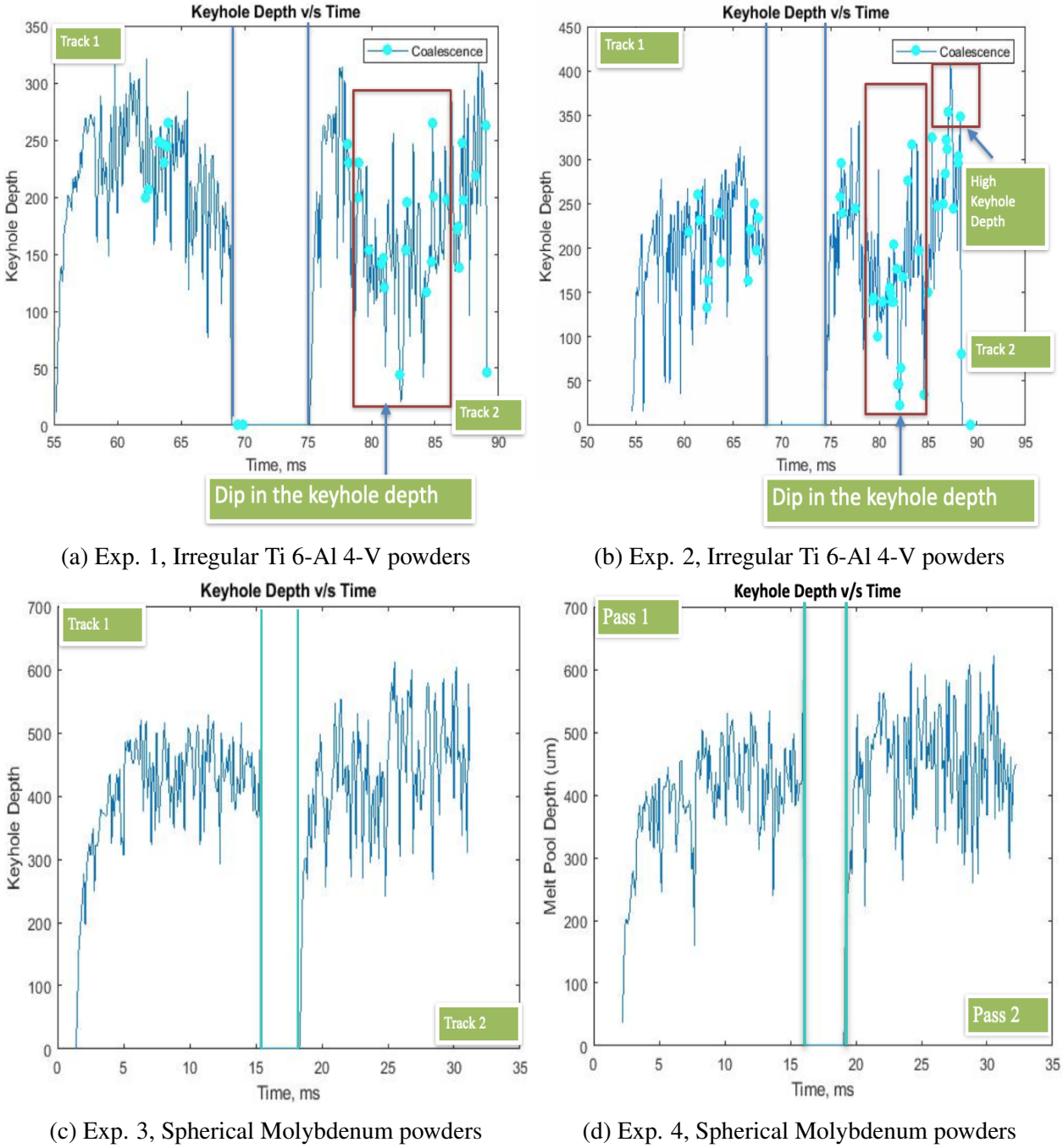

(a) Exp. 1, Irregular Ti 6-Al 4-V powders

(b) Exp. 2, Irregular Ti 6-Al 4-V powders

(c) Exp. 3, Spherical Molybdenum powders

(d) Exp. 4, Spherical Molybdenum powders

Figure 2.12: Keyhole Depth v/s Time

While there is no apparent correlation between coalescence and fluctuation in the keyhole depth. Exp. 1 and 2 do not show significant keyhole porosity regardless of their keyhole depth variation.

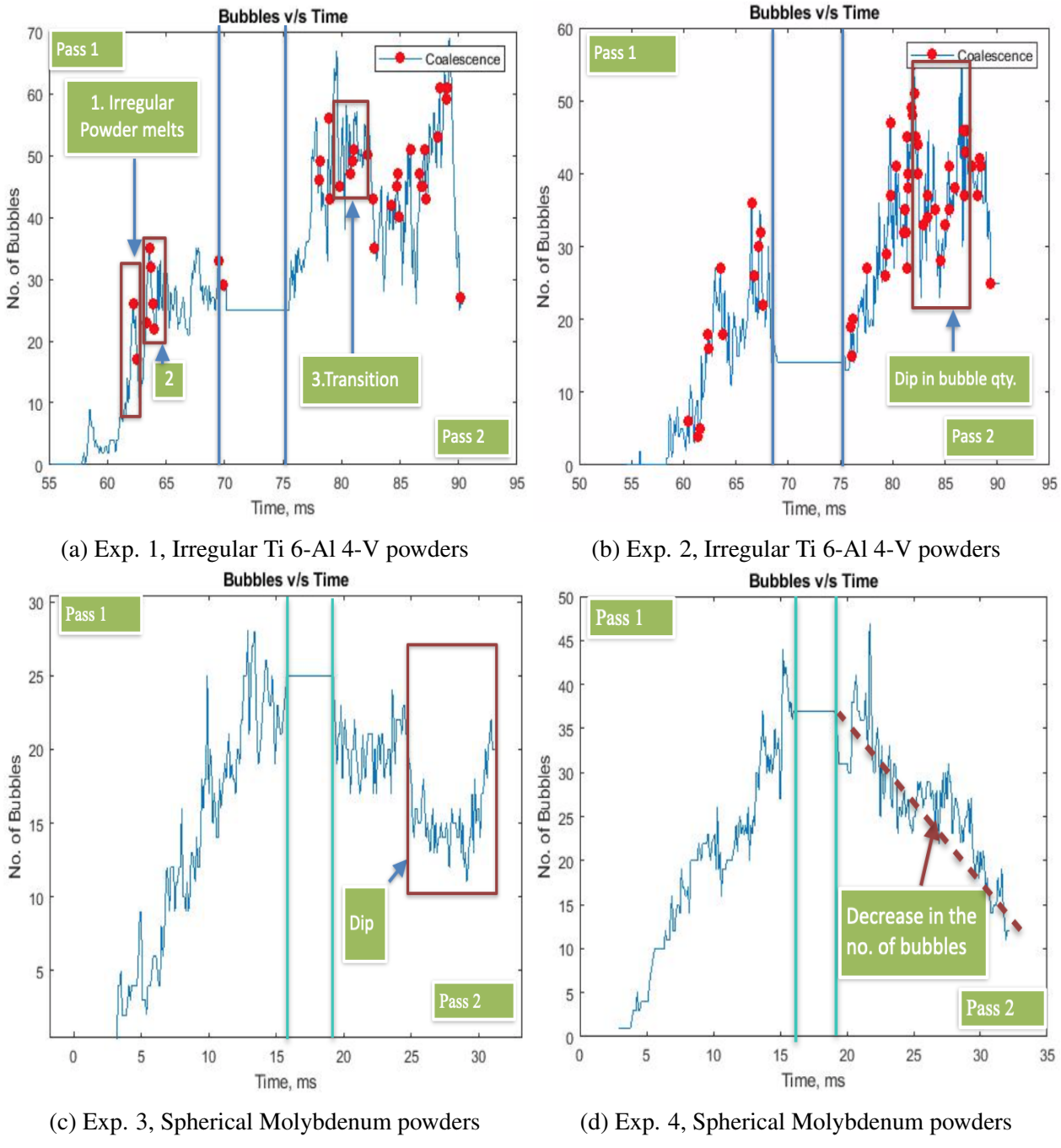

(a) Exp. 1, Irregular Ti 6-Al 4-V powders

(b) Exp. 2, Irregular Ti 6-Al 4-V powders

(c) Exp. 3, Spherical Molybdenum powders

(d) Exp. 4, Spherical Molybdenum powders

Figure 2.13: Bubble Quantity v/s Time

The quantity of bubbles present in the melt pool decreased as the second track progressed in Exp. 3 & 4 (Fig. 2.13c & 2.13d). This is interesting to note that while the keyhole instability is the most prominent mechanism for pore formation in exp. 3 & 4, there was no significant increase in pores formed. This does not conclude that keyhole porosity is uncorrelated with the fluctuation in keyhole depth. It should be noted that the fluctuation of keyhole depth in the second track maybe due to the re-absorption of pores to the bottom tip of the keyhole as, such instances, were observed while measuring the keyhole depths.

Fig. 2.13 shows the difference in the quantity of bubbles present in the melt-pool between Ti 6-Al 4-V powder and Molybdenum powder experiments. The mechanism of bubble formation in the Molybdenum experiments is through the keyhole instability due to the high power laser input used. Additionally, the use of spherical powders seems to facilitate the dominance of keyhole porosity that forms from the lowest tip of the keyhole. As the quantity of bubbles formed from this method depend on the ability of the keyhole to reach critical instability, the frequency of bubble formation is low. On the other hand, Exp. 1 & 2 have a larger quantity of bubble formed in the melt pool during the laser process. In these experiments, keyhole induced bubbles are dominantly formed at the edges of the keyhole.The keyhole edge cannot be as unstable as the keyhole tip at any given time, just, like the amplitude of vibrations at the edges of a string is always lower than that at the very center. A deeper look into the true mechanism of bubble formation at the edges of a keyhole traversing through partially fused powders would be beneficial. Another great contributor to spikes in bubble quantity was the fusion of irregular powders (see Fig. 2.14 and 2.15). Further research needs to be undertaken by isolating irregular powders to understand their influence on the formation of bubble clusters.

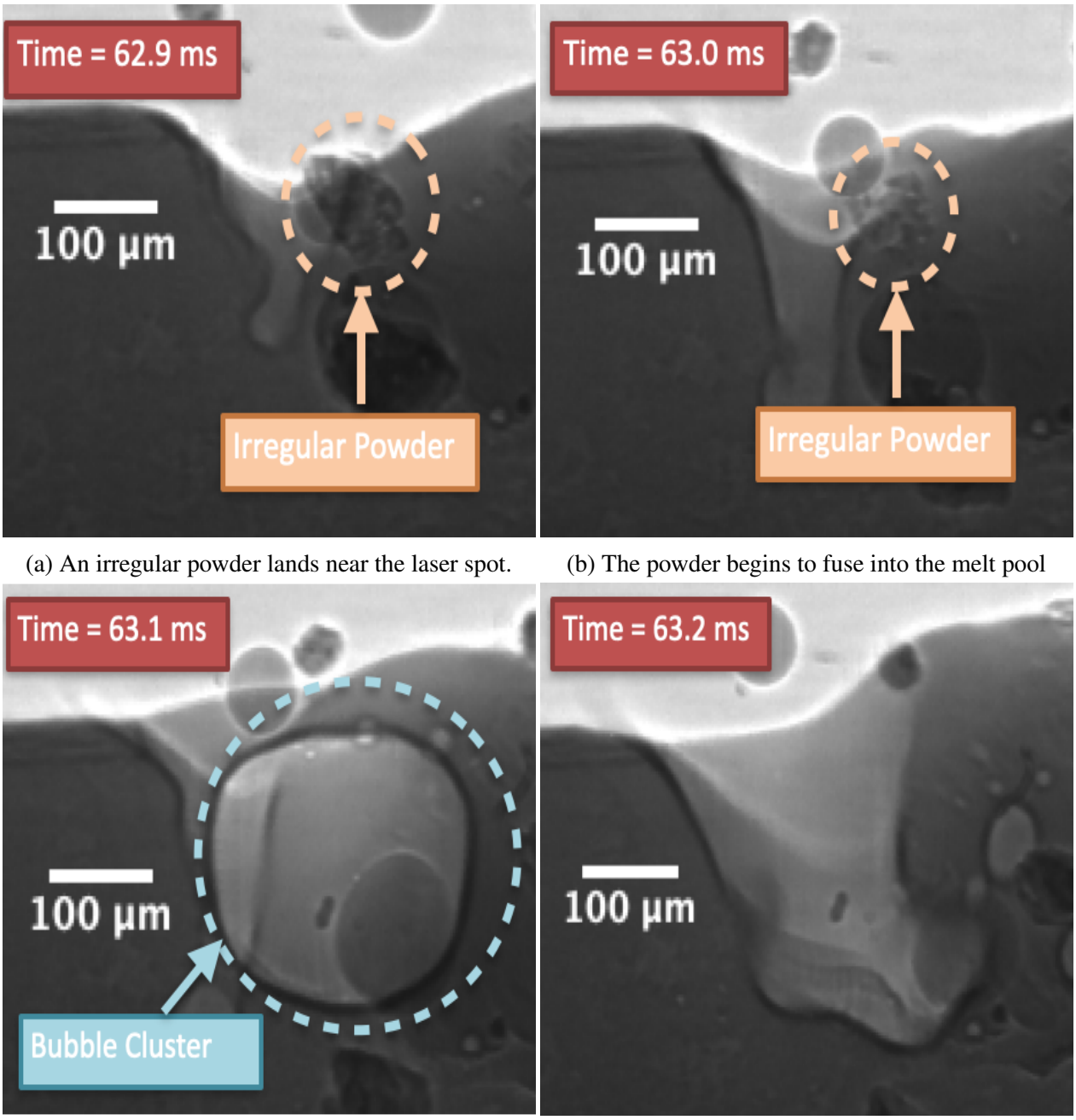

(a) An irregular powder lands near the laser spot.

(b) The powder begins to fuse into the melt pool

(c) A large bubble replaces the fused powders and is close to the keyhole. A few smaller bubbles surround the larger bubble

(d) The larger bubble is engulfed into the keyhole, whereas, the smaller bubbles endear and more bubbles are formed

Figure 2.14: Fusion of an irregular powder into the melt pool creates a large bubble surrounded by smaller bubbles, this disturbance in the melt pool creates the cluster of bubble seen in subsequent frames (Fig. 2.15). (The time steps are 0.1 ms, which is equivalent to 3 X-ray frames, while the starting point is when the IR camera starts.)

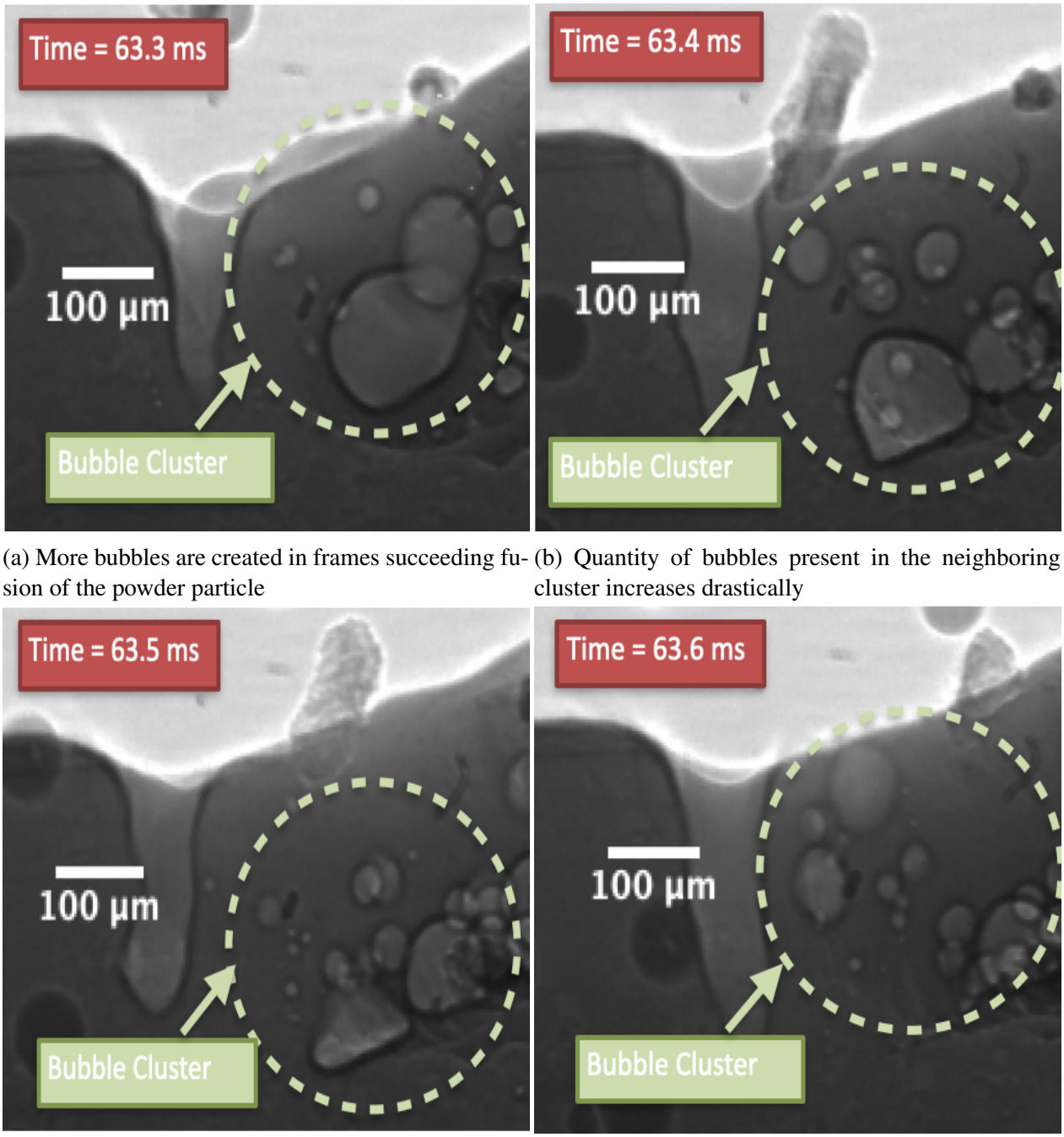

(a) More bubbles are created in frames succeeding fusion of the powder particle

(b) Quantity of bubbles present in the neighboring cluster increases drastically

(c) Smaller bubbles appear from wake of the keyhole

(d) A final dense cluster is seen

Figure 2.15: Irregular Powder fusion into the melt pool from Fig. 2.14 leads to a cluster of bubbles formed in subsequent time steps which create the second spike in bubble quantity seen in Fig. 2.13a. (The time steps are 0.1 ms which is equivalent to X-ray frames, while the starting point is when the IR camera starts.)

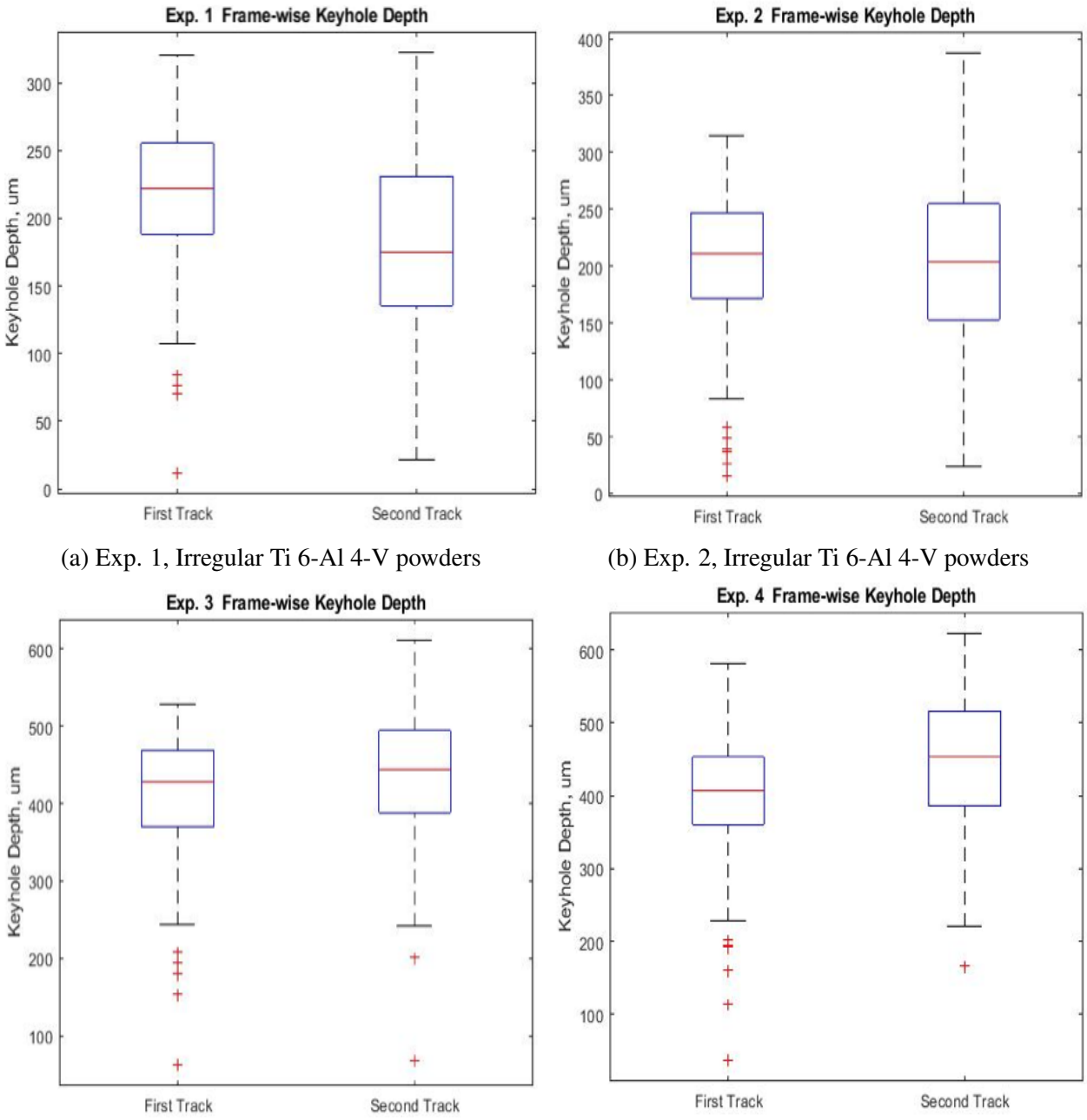

(a) Exp. 1, Irregular Ti 6-Al 4-V powders

(b) Exp. 2, Irregular Ti 6-Al 4-V powders

(c) Exp. 3, Spherical Molybdenum powders

(d) Exp. 4,Spherical Molybdenum powders

Figure 2.16: Distribution of keyhole depth in each X-ray frame

In Exp. 1, there were more bubbles formed in the earlier section of the second track. These bubbles were formed preceding the keyhole. As the keyhole proceeds between 80 ms and 82 ms, there is a transition region where the bubble formation preceding and succeeding the keyhole is

similar. After the transition region, a significant majority of the bubbles are formed succeeding the keyhole. These bubbles are relatively fewer in quantity but larger in size. This size difference between bubbles formed preceding and succeeding the melt pool is because whenever a large bubble was formed in front of the keyhole, it was absorbed into the keyhole, whereas, those formed succeeding it had more room to avoid the keyhole and subsequently settle far behind the keyhole.

Even as the parameters in Exp. 1 & 2 are same, there is a stark difference between the form of their bubble quantity versus time plots (Fig. 2.13a & 2.13b). The delay in the increase of the bubble quantity in Exp. 2 (Fig. 2.13b), is due to the position of the partially fused powders, which are farther away from the starting point of the second track in Exp. 2 as compared to Exp. 1. Thus, the location of partially fused powders seems to further dictate the formation of bubbles. Fig. 2.16 shows the dispersion of keyhole depths through out the experiments. The depth of keyhole was calculated every 3 X-ray frames, i.e, every 0.1 ms. Fig. 2.16a and 2.16b show a larger dispersion in the keyhole depths as compared to fig. 2.16c and 2.16d, this as seen earlier is due to the dip in the keyhole depths during the central region of the keyhole. Whereas, the keyhole depth fluctuates without a dip in the values.

The keyhole depth outliers present in the first tracks of all experiments belong to frames immediately following start of laser beam. Thus, they have lower values than that of the entire track.

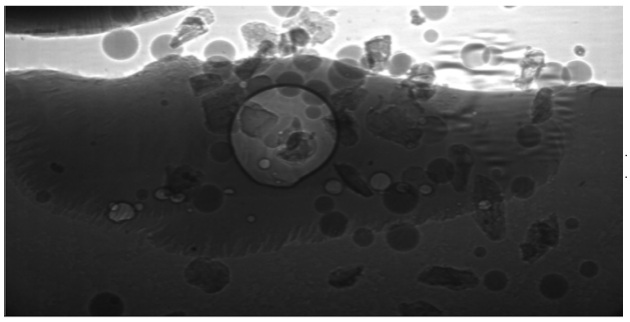

(a) Exp. 1, Irregular Ti 6-Al 4-V powders with 400 ms gas pulse and a low powder feed rate during the first laser pass

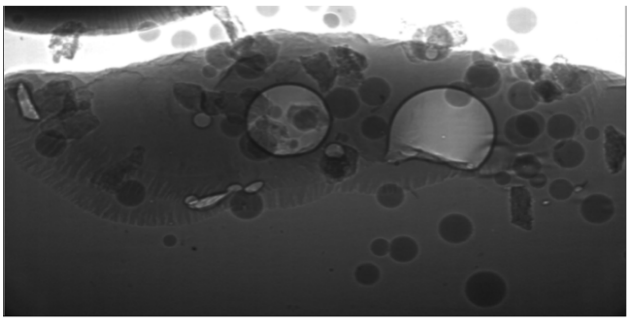

(b) Exp. 2, Irregular Ti 6-Al 4-V powders with 400 ms gas pulse and a high powder feed rate during the first laser pass

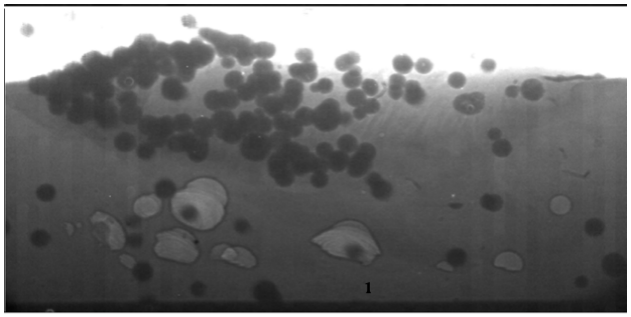

(c) Exp. 3, Spherical Molybdenum powders with 400 ms gas pulse and a low powder feed rate throughout the experiment

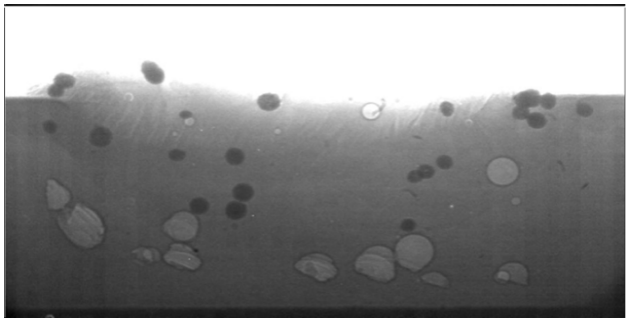

(d) Exp. 4, Spherical Molybdenum powders with 1000 ms gas pulse and a high powder feed rate throughout the experiment

Figure 2.17: Porosity after two laser scans,(a) We observe a spike in the no. of bubbles early on during the second pass (Fig. 2.13a), whereas, (b) has fewer pores (Table 2.2) and a larger median diameter. Pores in the Molybdenum experiments (c) & (d) were formed due to keyhole instability (All images are 1.75 mm wide)

Table 2.2: Final Pore effective diameters

Statistic	**1**	**2**	**3**	**4**
Quantity of pores (nos.)	27	12	20	23
Mean (μm)	40.34	89.41	65.35	80.88
Standard Deviation (μm)	60.55	95.17	49.46	45.04
Median (μm)	24.03	49.695	71.32	74.13
Deposition Delay (s)	0.79	0.79	0.9	0.9

Fig. 2.17 shows the final porosity after both the tracks are laid. It can be seen that the quantity of pores in both the Ti 6-Al 4-V experiments are differ greatly. The processing parameters for both the experiments is the same however, the partially fused powders were spread out differently in both the cases. The keyhole depth fluctuated however, there is a difference in the pulse phase at which powders enter the melt pool. Due to the pulsed powder feeder, Exp. 1 received most of its powder at the very end of the laser first laser track. Thus, most of the powders sprayed during the first laser track never fused.

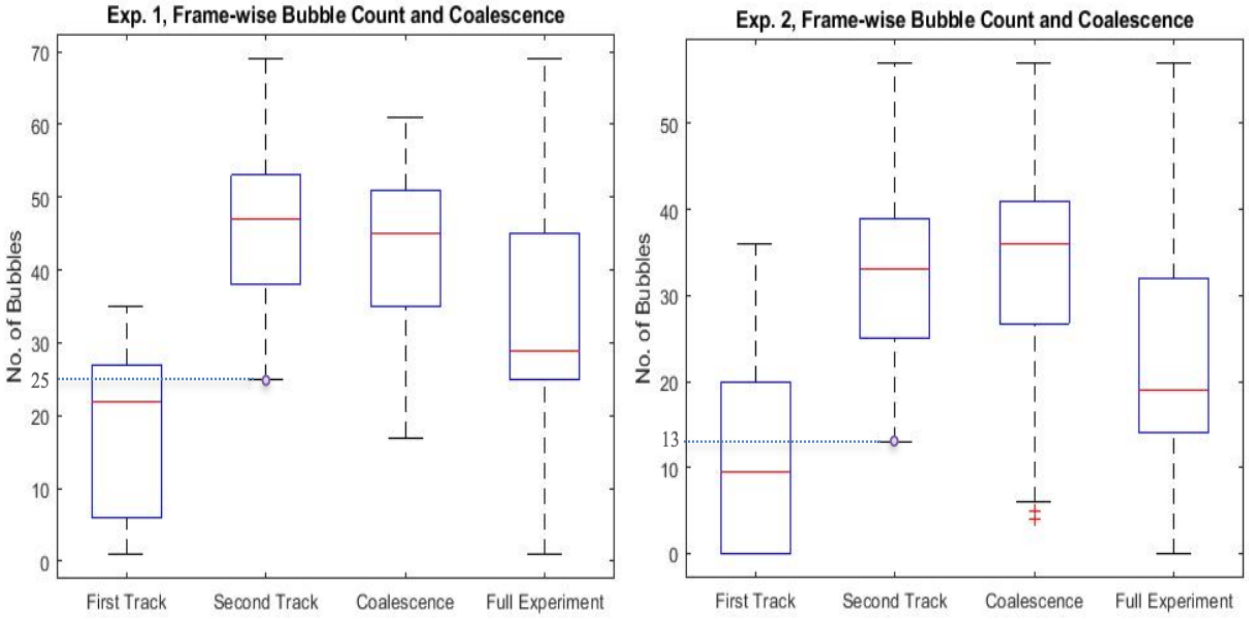

(a) Exp. 1, low powder feed rate during the first laser pass

(b) Exp. 2, high powder feed rate during the first laser pass

Figure 2.18: Quantity of bubbles present in the melt pool for each 0.1 ms during the first pass, second pass, frames during which coalescence occurred and the entire experiment.

As seen in Fig. 2.17 and shown in Table 2.2, there is a larger standard deviation in the final pore diameters after two tracks. The standard deviation for exp 2 is higher because there are more pores with larger diameters. Whereas, exp. 1 has only one large pores and the other pores are greatly smaller than it. In exp. 1, there are 3 instances of coalescence that lead to large bubbles,

out of which only one bubble survives, the surviving bubble is formed when the laser is near the end of its second pass. The other two bubbles burst due to penetration by a powder and the melt pool dynamics respectively. While bubble coalescence leads to 3 large bubbles in exp. 2 as well the first bubble sinks deep into the melt pool, further shrinking to form an irregularly shaped pore. The other two large bubbles in exp. 2 form the final part porosity.

Fig. 2.18 shows the difference in the quantity of bubbles present in the melt pool between the first pass and second laser pass. More bubbles are present in the melt pool during each frame of the second pass as compared to the first pass. This is partially due to the existence of 25 bubbles available from the first pass in exp. 1 and 13 bubbles retained in exp. 2. Exp. 1 does see a larger quantity of bubbles present in the melt pool with a maximum of 69 bubbles seen 34.0 ms after the laser starts its first pass. A surge in the quantity of bubbles present in the melt pool is observed earlier during the 1^{st} pass of exp. 1. The spike in bubble quantity which is highlighted as the 1st point of interest in Fig 2.13a is due to the melting of an irregularly shaped powder, which had landed very close to the keyhole. This surge is short lived once the effect of melting the powder is seen. The bubbles formed during the surge settle at the bottom of the melt pool and 3 instances of coalescence are observed which facilitate the reduction in bubbles. The following surge in quantity of bubbles seen in the 2^{nd} pt. of interest in Fig 2.13a are due to bubbles formed in the wake of the keyhole, though no influence of powder is noticed in these frames. This is followed by a quieter melt pool where scant bubble formation is dominant. Additionally, between 64.5 ms and 67 ms, a majority of the newly formed bubbles burst a few frames after they are formed due to melt pool dynamics.

Thus, we see that a higher quantity of bubbles present in the melt pool during the printing process contributes to the phenomenon of coalescence. While this phenomenon is trivial. A careful attention to the formation mechanisms of bubbles in the irregular Ti 6-Al 4-V powder experiments and spherical Molybdenum powder experiments shows us the tendency of Ti 6-Al 4-V experiments to have coalescence. This increase in the presence of bubbles in the Ti 6-Al 4-V experiments can be due to the bubbles carried into the melt pool by the irregular powder when the penetrate the melt

pool as well as the porosity inherent into the irregularly shaped bubbles. The Ti 6-Al 4-V powders had the same melting point as the substrate.

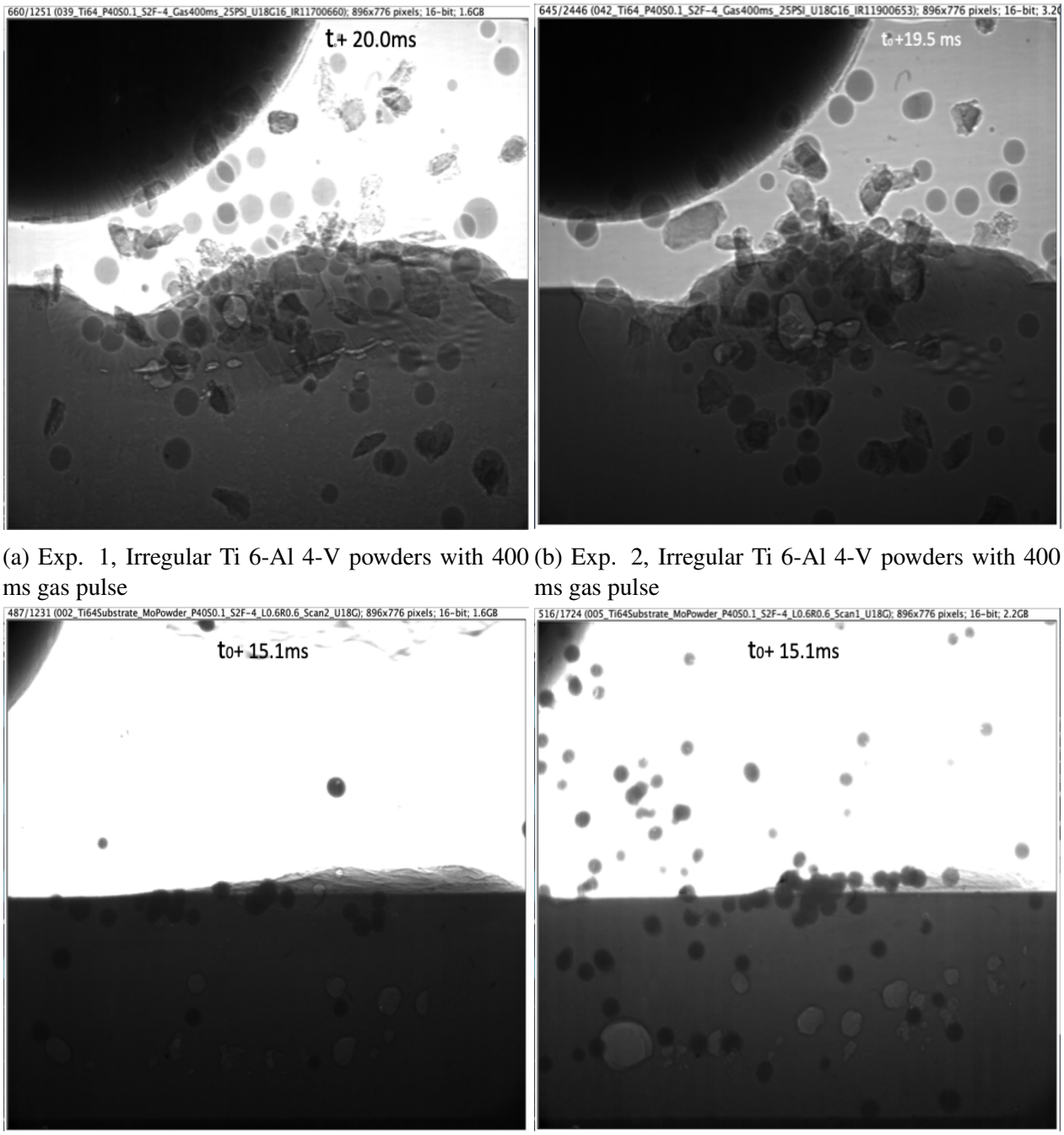

(a) Exp. 1, Irregular Ti 6-Al 4-V powders with 400 ms gas pulse

(b) Exp. 2, Irregular Ti 6-Al 4-V powders with 400 ms gas pulse

(c) Exp. 3, Spherical Molybdenum powders with 400 ms gas pulse and a low powder flow rate

(d) Exp. 4, Spherical Molybdenum powders with 1000 ms gas pulse and a high powder flow rate

Figure 2.19: Surface topography after first laser pass

The irregular shape of the Ti 6-Al 4-V powders, increase the irregularities on the surface of the substrate which trapped powders on the surface of the substrate (Fig. 2.19a & 2.19b). This increased the presence of lose and partially fused irregular powders on the surface making the surface irregular and rough. During the second laser pass of Ti64, the following factors contributed to an increase in bubbles present in frame and more instances of coalescence: surface roughness due to the irregular shape of powders present on the surface as well as the incoming powders, the pores formed in the first laser pass and the laser power used melt the powders. Additionally, the powder flows into the melt pool of the first laser pass more frequently in Exp. 2 as compared to Exp. 1. This was the only drastic difference observed between these experiments which may have led to the difference in the quantity and size of pores formed in these experiments.

Molybdenum powders had a smaller average size than the Ti 6-Al 4-V experiments, were spherical in shape and had a higher melting point. The smaller size and spherical shape of Molybdenum powder allowed the powders to enter the melt pool without causing the bubbles to form. Additionally, since the Molybdenum powders barely fused, there were no bubbles formed due to the inclusion of powders. At the end of the first laser pass, the Molybdenum powders did not reside on the surface of the substrate to the amplitude that was seen in the Ti 6-Al 4-V experiments(Fig. 2.19c & 2.19d). Exp. 3 had a lower powder flow rate throughout the experiment. Thus, for the second laser pass as well, keyhole instability was the only major mechanism of bubble formation. Hence, in the Molybdenum experiments we do not see huge spikes in the quantity of bubbles present in the melt pool.

2.6.4 Contact time for coalescence

Fig. 2.20 shows the distribution of the contact times between Exp. 1 and Exp. 2. There were 34 instances of coalescence in Exp. 1 and 55 in Exp. 2. The minimum and maximum contact times for coalescence is similar. However, many bubbles stayed in contact longer than most contact times without coalescence. The drainage time is dependent on the respective bubble diameters, velocity of approach and properties of the surrounding liquid [51, 50, 44].Thus, future studies are required to categorize coalescence based on their respective drainage times.

As seen in the plots, coalescence takes place usually after 1-9 frames of being in contact. The median of around 5 & 4 frames shows that a majority of coalescence takes place rapidly. This amounts to approximately 166.66 μs and 133.36 μs respectively. There are many bubbles that reside in the melt pool in contact with one another however, do not coalesce. Additionally, it is commonly thought that coalescence takes place if the approach velocity between the bubbles is optimal. However, in the above experiments coalescence occurred even if the bubbles were stationary close to each other, however, the oscillations formed on the surface of the bubbles lead to coalescence between neighboring bubbles. Additionally, longer instances of coalescence take place when the bubbles are in contact with one another but there is no apparent relative velocity component that pushes the bubbles against one another.

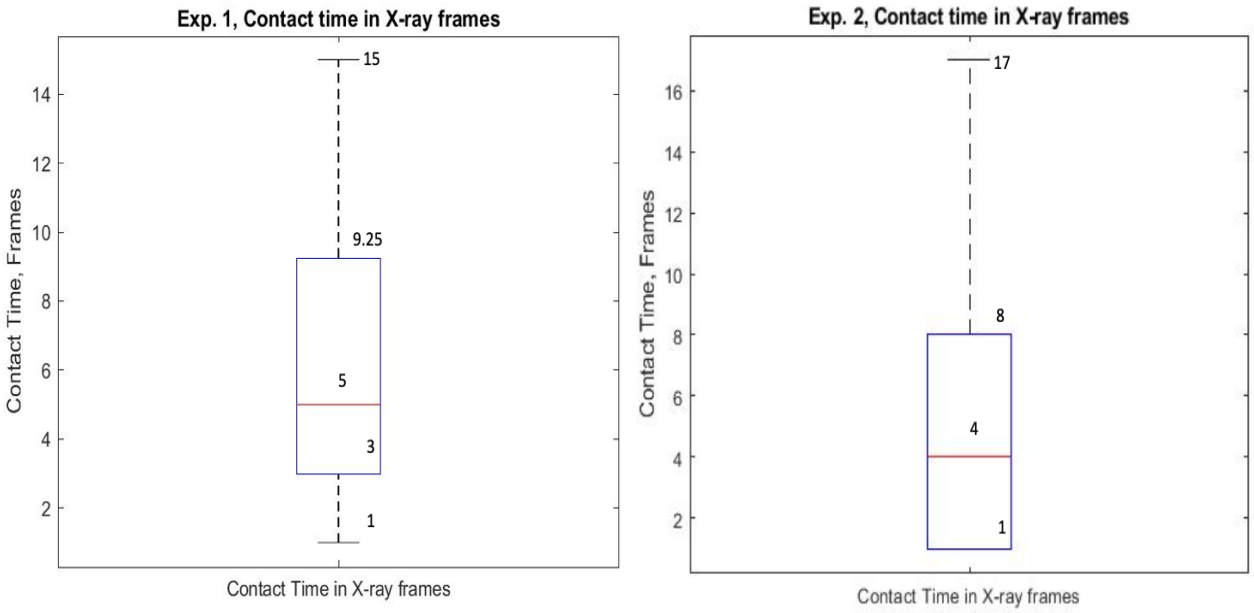

(a) Exp. 1, Low powder feed rate during the first laser pass

(b) Exp. 2, high powder feed rate during the first laser pass

Figure 2.20: Contact Time distribution for experiments with irregular and spherical Ti 6-Al 4-V powders on Ti 6-Al 4-V substrate. (Each frame amounts to 33.33 μs)

As seen in Fig. 2.20, the contact times that lead to coalescence are all above 1 frame (33.33

μs).

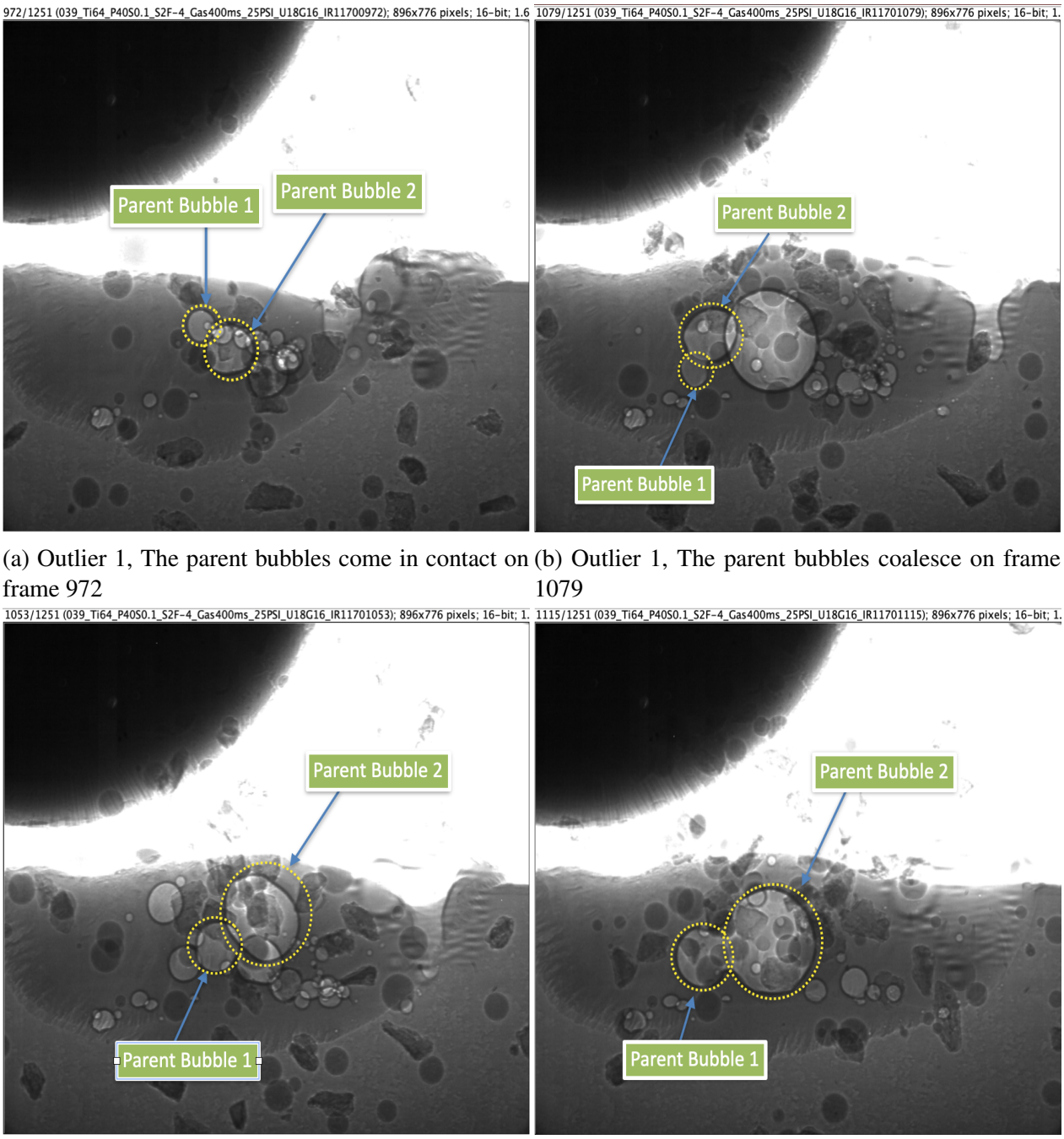

(a) Outlier 1, The parent bubbles come in contact on frame 972

(b) Outlier 1, The parent bubbles coalesce on frame 1079

(c) Outlier 2, The parent bubbles come in contact on frame 1053

(d) Outlier 2, The parent bubbles coalesce on frame 1115

Figure 2.21: Contact time for outliers observed in Exp. 1, irregular and spherical Ti 6-Al 4-V powders on Ti 6-Al 4-V substrate

Out of the three commonly used models to predict coalescence, the energy and velocity models do not use the mechanics of coalescence and predict coalescence using generalised concepts. In the experiments analysed, there were 16 occurrences of coalescence with the contact time of 33.33 μs in total, which is the lowest resolution seen. Whereas, there were 89 instances of coalescence in total. All the instances of coalescence saw parent bubbles come in contact with each other for at least 33.33 μs before coalescence. Thus, the film drainage time can be calculated for these instances of coalescence. As the film drainage model utilises the mechanics involved in coalescence, it is theoretically the best approach to model coalescence in this time scale.

Two outliers were observed in Exp. 1. They required 107 and 61 frames to coalesce, they were removed from the box plot values to show the distribution clearly. The outliers are shown in Fig. 2.21. These parent bubbles come in contact near the end of the second laser pass. Additionally, these bubbles are present in the wake of the keyhole, where the melt pool can preserve larger bubbles. These parent bubbles do not appear move closer to one another until they coalesce. These bubbles move farther away from the keyhole rotate about the axis of the larger bubbles. The smaller bubble does not detach from the surface of the larger bubble until they coalesce.

Table 2.3: Coalescing Bubbles size statistics

Statistic	**1**	**2**
Quantity of coalesced bubbles (nos.)	34	55
Standard Deviation (μm)	56.02	62.92
Median (μm)	100.87	85.21

The bubbles that coalesce have a relatively larger diameter than other. Bubbles with diameter less than 10 μm did not coalesce. This may have been due to their higher internal pressure and corresponding higher surface energy which is difficult to break.

2.7 Conclusion

The final part porosity after the directed energy deposition method of metal additive manufacturing consists of pores formed from bubbles that underwent morphological changes such as coalescence before it solidified into a pore.

- Coalescence requires a higher bubble density which was present in the Ti 6-Al 4-V powder experiments. The experiments that used spherical Molybdenum powders saw a lower bubble density during the process.
- Clusters of bubbles were seen succeeding the fusion of an irregular powder in Ti 6-Al 4-V experiments.
- Exp. 1 & 2, which used Ti 6-Al 4-V powders, saw a collection of new powders on the surface. This may have been due to the increase in surface roughness caused by the partial fusion of irregular powders on the substrate.
- The partially fused powders led to higher bubble density in the molten pool during the second laser passes for Exp. 1 & 2.
- Exp. 1 & 2 saw a greater variation in the keyhole depth during their second laser passes. This was due to the increase in powder accumulation as well.
- The contact time required for coalescence was between 0.033 ms and 0.561 ms.
- As each instance of coalescence occurred after at least one visible X-ray frame of contact between the parent bubbles. The film drainage model is feasible for future research at the current time scale.

2.8 Future Work

Using in-situ X-ray imaging, we get a better insight into the morphological evolution of bubbles in metal directed energy deposition from their birth until solidification, with many possibilities

for future experiments. The experiments used above belonged to two different feed-stock material types. The Ti 6-Al 4-V feed-stock material had a mixture of irregular and spherical powders, while the Molybdenum powders were spherical in shape. Further research needs to be undertaken to study the degree of influence that shape powders have on bubble cluster formation. Additionally, more laser passes should be considered to analyse the evolution of porosity after the formation of large pores due to coalescence. The influence of partially fused powders on bubble density in consequent laser passes should be analysed in using a proper design of experiments. Further research can use partially fused powders to create bubble concentration hubs which can be destroyed using localized re-melting. This is better than re-melting the entire surface. Further research should focus on using powder flow and laser power to control the location of coalescence.

The contact time before bubble coalescence needs to be quantified for different materials and alloys. Additionally, the influence of magnetic field to manipulate the melt pool should be further studied in order to coalesce bubbles in a more controlled manner.

3. INFRARED EMISSIVITY ESTIMATION

3.1 Motivation

The bubble coalescence detected by the in-situ X-ray imaging can be synchronized with other in-situ sensing techniques that are more relevant to industrial applications. Thermal characteristics of the melt pool have a huge impact on the liquid and gas attributes such as surface tension, flow fields, gas pressure etc. Solidification of the melt pool can also be observed using in-situ thermography, which is common in commercial DED machines. All these are influence the bubble dynamics inside the melt pool. Additionally, thermal sensing equipment have been widely proliferated in the additive manufacturing community.

Thus, to control the bubble dynamics in-situ, a causal relationship between the surface temperature of the melt pool and the bubble characteristics need to be found. As a first step into this deeper study, the thermal images taken from the infrared camera during the additive manufacturing process needs to be calibrated to give its users an accurate temperature reading. Infrared pyrometers are widely used for thermal sensing. Additionally, for high-speed imaging with a high enough resolution to detect the radiation from points of coalescence, infrared pyrometers are a perfect choice.

This research makes an attempt to calibrate the infrared images using a scaling factor called emissivity to extract the actual temperatures of the surface of the melt pool. The emissivity is calculated dynamically, i.e for every 0.1 ms.

3.2 Methodology

Exp. 1 from Chapter 2 was used to conduct this study. The raw data was downloaded from Dr. Wolff's Box drive. To convert the raw data to IR images, MATLAB scripts provided by Dr. Wolff were used. Once the IR images were created as TIFF files and stored in a folder, pixel temperatures were extracted from them by using the "imread()" function in MATLAB

To calculate the emissivity of an object by using a known surface temperature on the object,

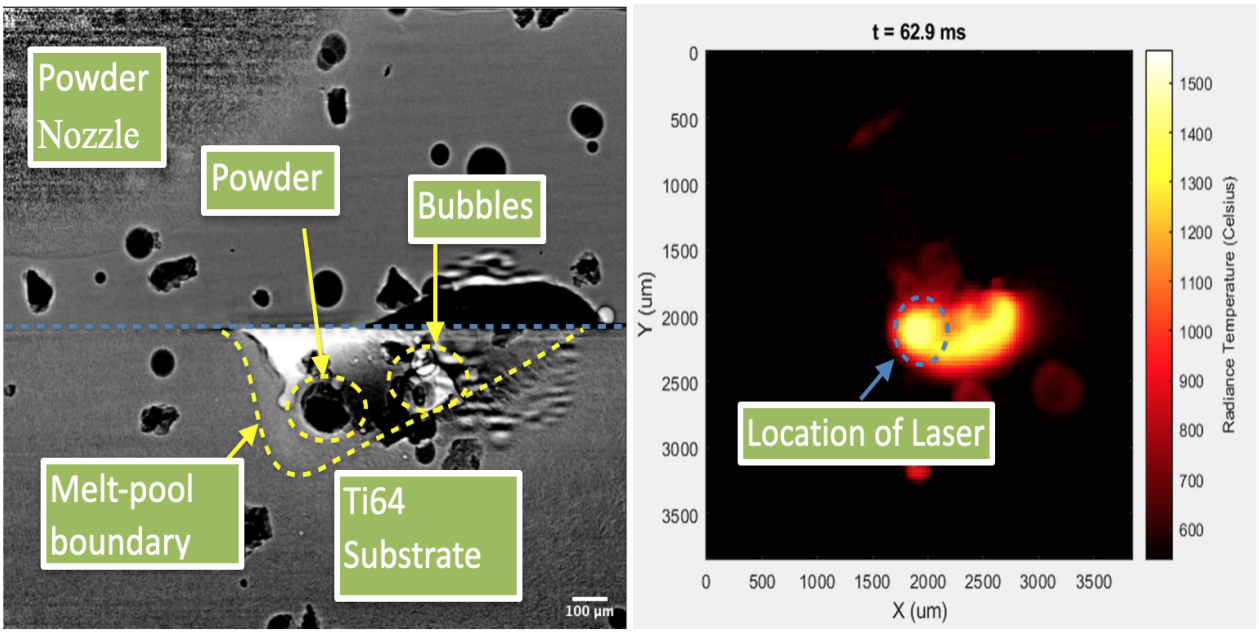

(a) Divided X-ray image

(b) Infrared image

Figure 3.1: (a) Image cleaning done by dividing the X-ray frame under consideration by background image (Fig. 2.4a) to visualise the melt-pool boundary distinctly (b) The infrared image as received from Dr. Wolff

the following equation was used [17, 52],

$$\epsilon = \left(\frac{T}{T_m}\right)^4 \tag{3.1}$$

where, "T" is the temperature of the object in consideration, "T_m" is the liquidus temperature of the material under consideration.

Eq. 2,3 and 4 were used to locate the melt-pool boundary, visible in the X-ray images, in the IR images. The boundary was located after every 3 X-ray frames to create a time-step of 0.1 ms.

The X-ray frame number was converted to the IR frame number by using the formula,

$$t_{IR} = \frac{f_{0_{IR}}}{10} + \frac{(t_{Xray} - t_{0_{Xray}})}{30} \tag{3.2}$$

. Where, t_{IR} is the time in the IR image measured in milliseconds, f_0 is the starting frame of the

laser in the IR stack, Whereas the x-coordinate from the X-ray was converted to the coordinate values in the IR image using,

$$x_{IR} = x_{Is} - \left(\frac{|x_X - x_{Xs}|}{|x_{Xs} - x_{Xe}|} \right) \times (|x_{Is} - x_{Ie}|) \tag{3.3}$$

$$y_{IR} = y_{Is} + \left(\frac{|x_X - x_{Xs}|}{|x_{Xs} - x_{Xe}|} \right) \times (|y_{Is} - y_{Ie}|) \tag{3.4}$$

In Eq. 3.3 and 3.4, Is and Ie are used to label the laser starting and ending points in the infrared (IR) frames respectively, where x and y are the x-coordinate and y-coordinate respectively. Similarly, Xs and Xe are used to describe starting and ending points of the track as seen in the X-ray images. IR labels the position of coalescence in the IR image, the value was divided by 30 to get the IR image pixel at which coalescence takes place. These calculations were done on "Numbers" software by Apple Inc.

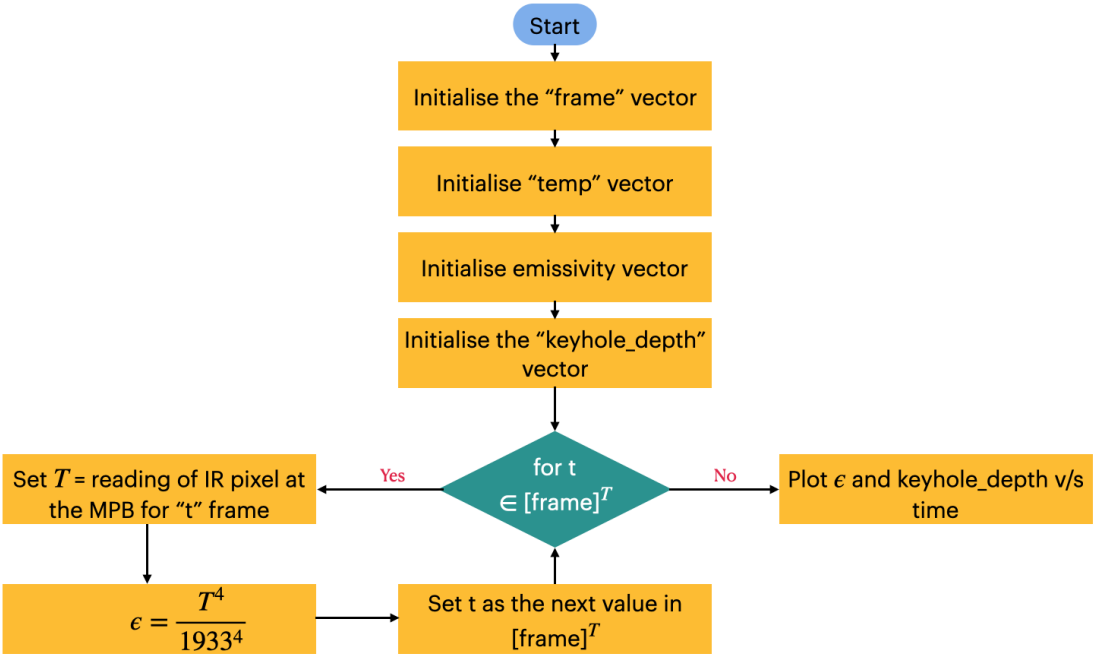

Figure 3.2: Calculating the emissivity for each frame and plotting the results along with the keyhole depth v/s time

MATLAB was used to perform the calculations and Fig.3.2 shows the flowchart used to calculate the emissivity of each frame under inspection. To calculate the emissivities using the above formulae, a "frame" vector was created which consisted of each frame number where the laser was turned ON and the melt pool boundary was clearly visible. The "temp" vector consisted of the radiometric temperatures (T), for each frame in the "frame" vector, measured from pixels at the melt pool boundary (MPB). Emissivity vector is a vector consisting of the emissivity for each frame under consideration, where, "ϵ" is the emissivity for the current frame in the for loop. The "keyhole_depth" vector consists of the depth of the keyhole in μm for each frame.

Surface temperature at the melt pool boundary was used to create a threshold for the melt pool boundary. This threshold was used to make the image binary where each pixel with temperature higher than that of the melt pool boundary is high while the others are low. The melt pool boundary was traced using the "bwboundaries" function in MATLAB.

3.3 Results

As shown in Fig. 3.3, the emissivity values differ greatly between the first and second laser passes. However, the value of emissivity fluctuates to a lesser extent during the solidification period of the laser while the emissivity is still higher than the mean emissivity during the first laser pass. The emissvity is dependent on the wavelength of light measured and the equipment used in the experiments. According to the manufacturer, the Telops Fast M3K infrared camera used by B Gould et al. [17] has a wavelength range of 1.5-5.4 μm. However, in the research conducted by Gonzalez et al. [53], the infrared emissivity of Ti 6-Al 4-V should be near 0.2 for the higher spectral threshold of the IR camera. These values of emissivity were calculated only uptil 1100K, while the melting point under consideration is 1933 K. The emissivity decreases with increase in temperature after reaching a peak at around 850 K [53]. Additionally, the liquid phase metals usually have a higher emissivity value [54]. The spectral emissivity should also increase with an increase in surface roughness due to the action of laser melting [55, 56]. However, the lower emissivity noted for the Ti 6-Al 4-V substrate in the first experiment may be due to the highly polished subrstrate used. The emissivity value fluctuates about a constant line with a mean

of 0.045 for the first laser pass. This is opposed to the change in emissivity observed throughout the second laser pass. Mean emissivity during the second laser pass was 0.2346. Thus, a change of 0.1996 was observed the mean emissivty between first and second laser pass. The standard deviation was 0.0167 and 0.0534 for the first and second pass respectively (Table. 3.1).

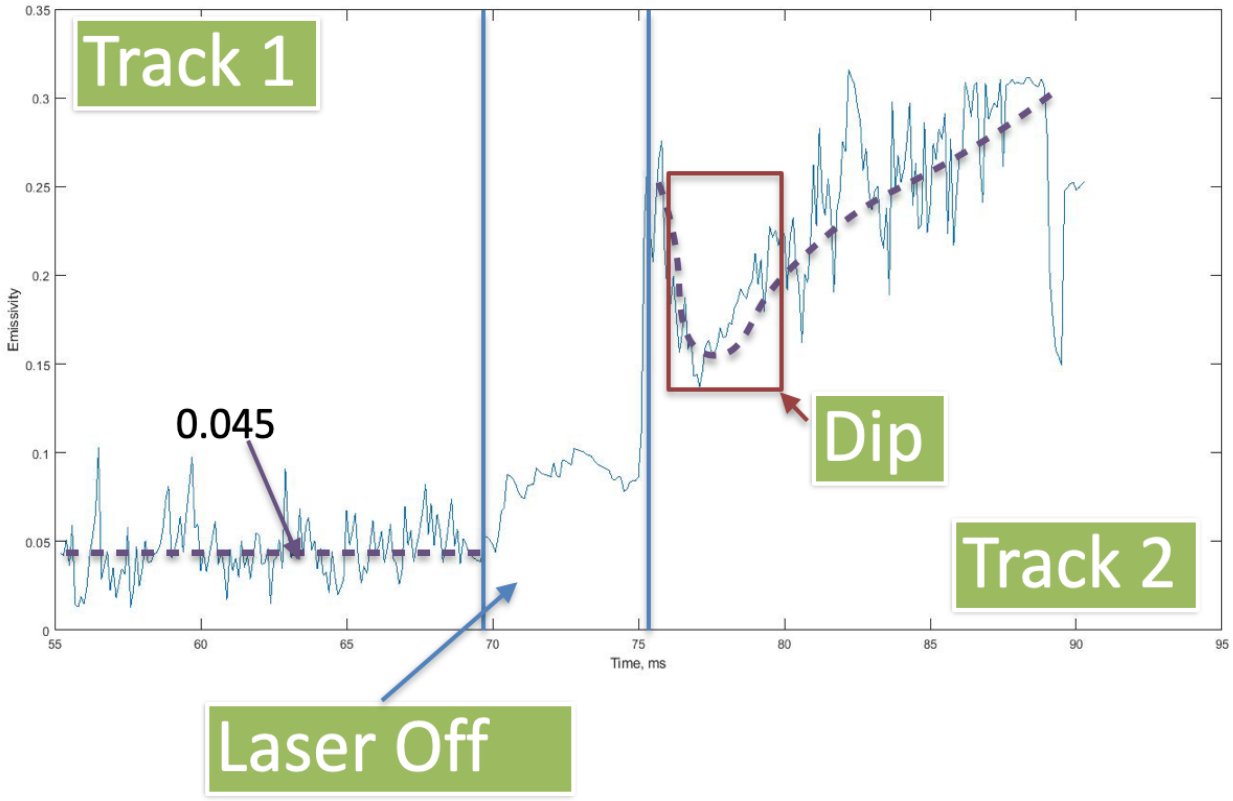

Figure 3.3: Emissivity v/s Time (ms) for Exp. 1

Table 3.1: Emissivity statistics between laser passes

Laser Pass	**First**	**Second**
Standard Deviation	0.0167	0.0534
Mean	0.045	0.2346

The boundary temp. was used as a threshold to create the melt pool boundary shown in Fig. 3.4a. The melt pool boundary of the first laser pass shows good approximation as with the liquid portion of the melt pool. However, the semi solid region is excluded. The liquid portion is approximated as the melt pool boundary leading the laser and the point where the surface stops moving in the wake of the laser 3.4a. However, the higher emissivity detected in the second laser pass, due to higher temperatures reached by the same input energy gives incorrect readings regarding the melt pool shape. In Fig. 3.4b, it shows two liquid pools on the surface, however, pool toward the right should not be present as the melt pool had solidified before the second laser pass started. This may be due to higher emissivity of the second laser track. The higher emissivity leads to higher intensity of the radiated infrared rays while the IR filter cuts off the radiometric temperature at 1567 K.

Effect of the interference caused by radiation from latent heat of solidification can be seen in Fig. 3.5. The dip in emissivity during the second laser pass is because the laser enters a depression on the surface made during the end of the first laser pass (Fig. 3.6a).

The radiometric temperature measured at leading edge of the melt pool is lower than that when measured after the dip. After the laser crosses first half of its second pass, radiation from the leading melt pool boundary increases as the latent heat of solidification emitted from the surrounding area adds to the heat from the boundary. This increase is shown in Fig. 3.5b. This high radiometric temperature used during thresholding leads to errors while determining the melt pool boundary as most of the surface is excluded from the estimated melt pool. This is a limitation of this process. The emissivity of first laser pass and the second laser pass have a huge difference and an appropriate infrared filter is needed to accurately measure the temperature of a melt pool boundary during the second pass.

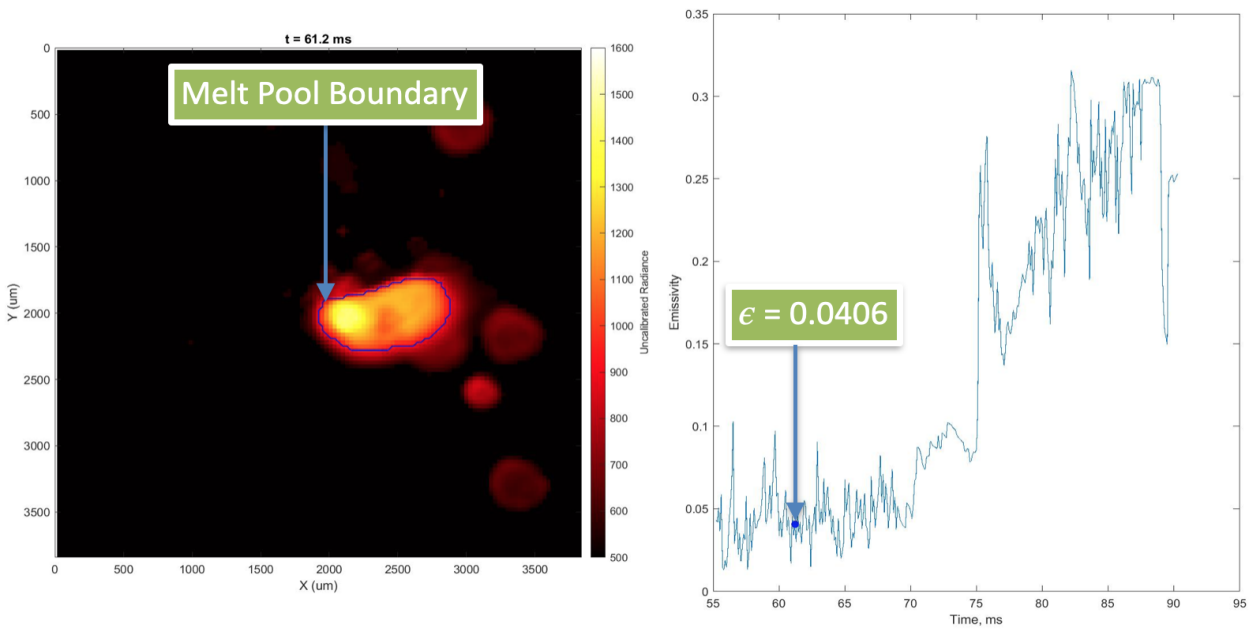

(a) The emissivity is 0.04, 61.2 ms after the IR camera starts

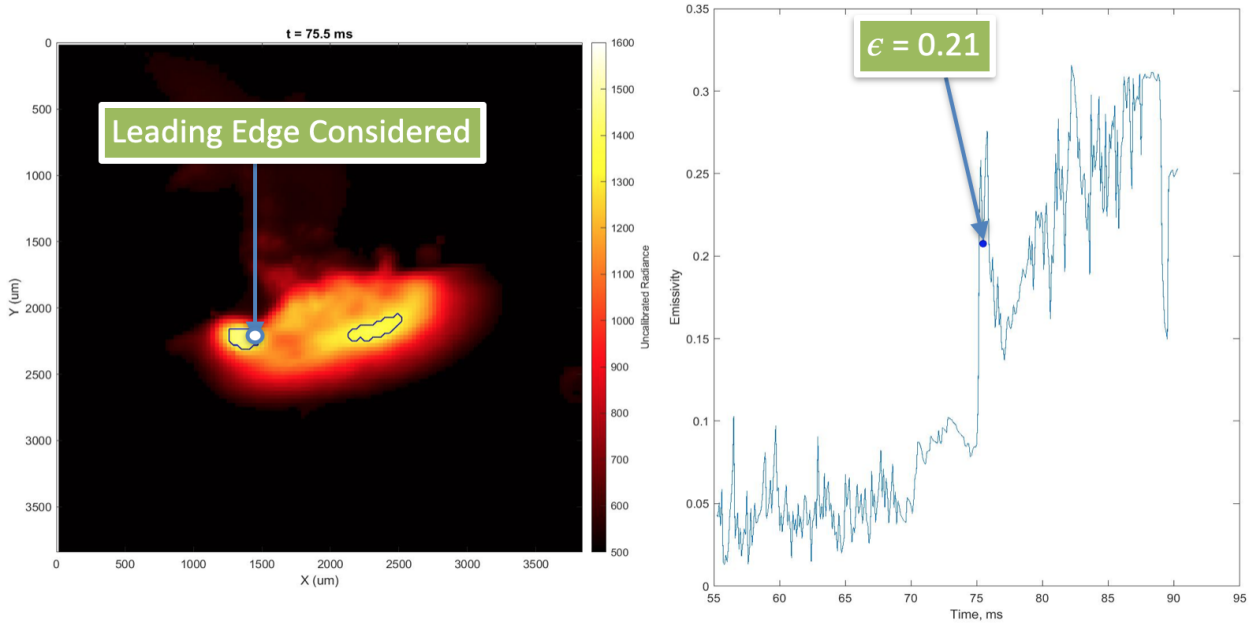

(b) The emissivity is 0.21, 75.5 ms after the IR camera starts

Figure 3.4: (Left) Uncalibrated IR image with melt pool boundary, (Right) Emissivity v/s Time (ms). (a) shows the first laser pass and (b) shows that during the beginning of second laser pass.

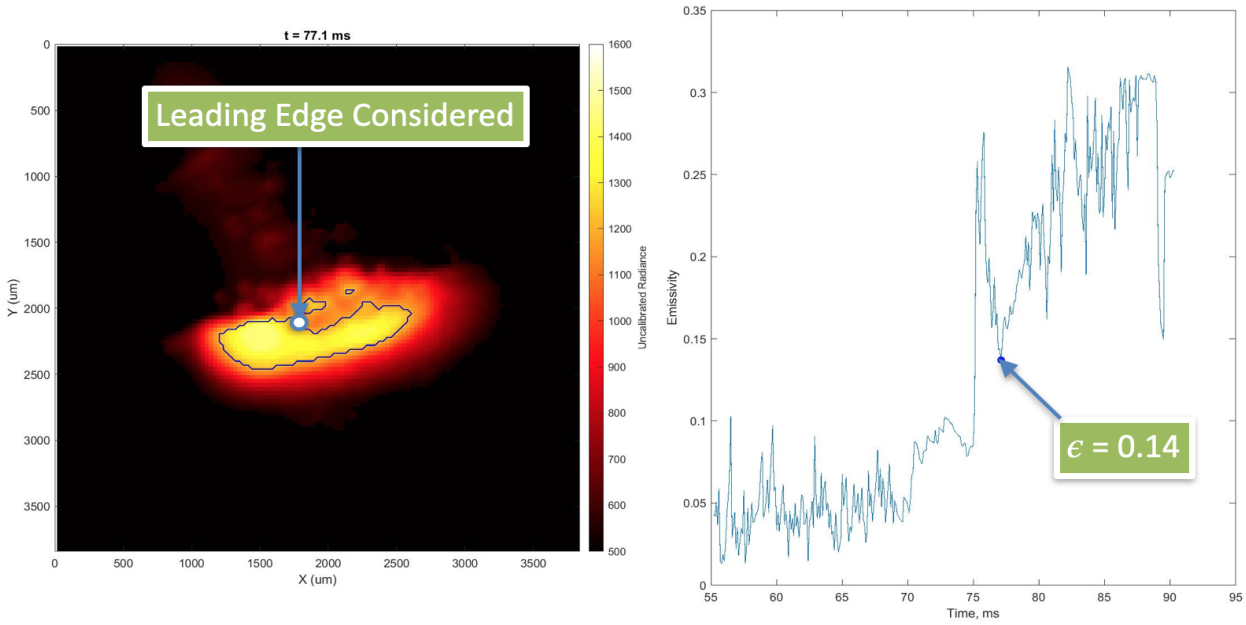

(a) The leading edge of melt pool is not interfered by the heat radiated by the latent heat of solidification

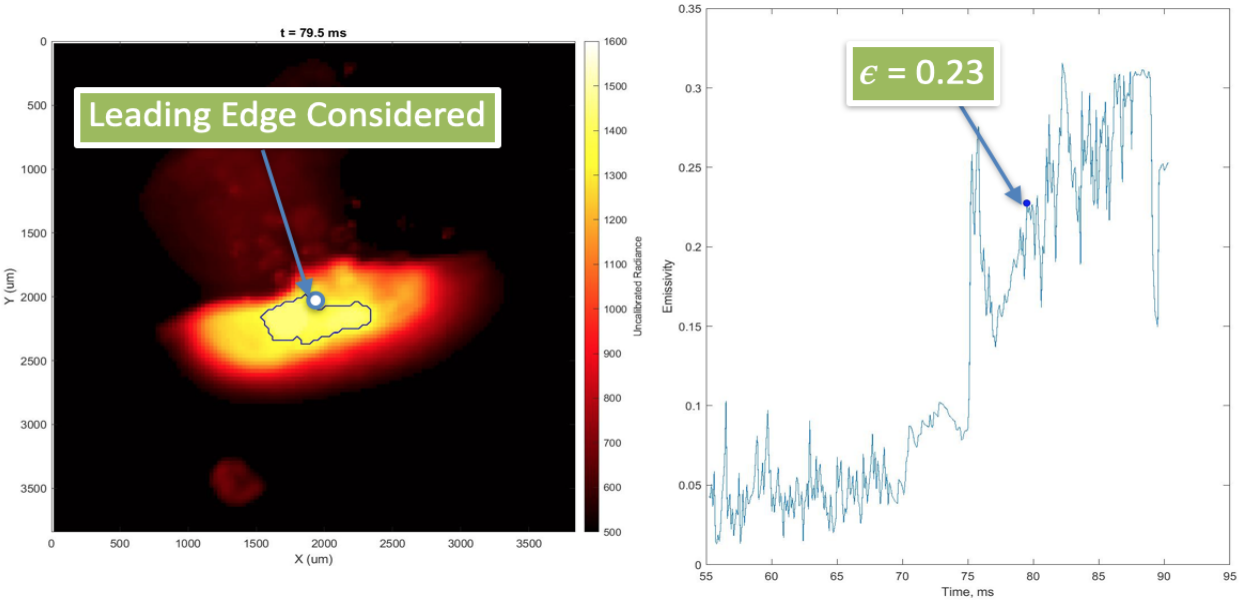

(b) The leading edge of melt pool is detected to be hotted due to interference from the heat radiated by the latent heat of solidification

Figure 3.5: Latent heat of solidification interferes with the radiometric temperature detected at the leading edge of the melt pool leads to incorrect melt pool detection during the second laser pass. Both (a) and (b) belong to the second laser pass

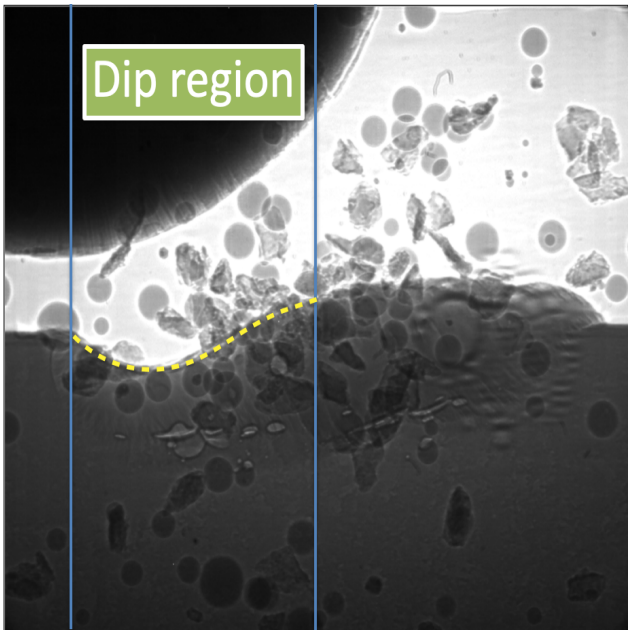

(a) The depression created at the end of the first pass

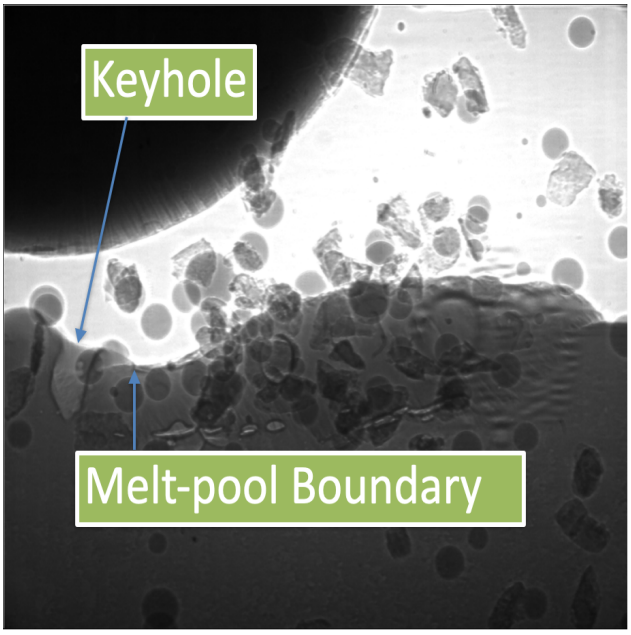

(b) The laser starts to enter the depression region

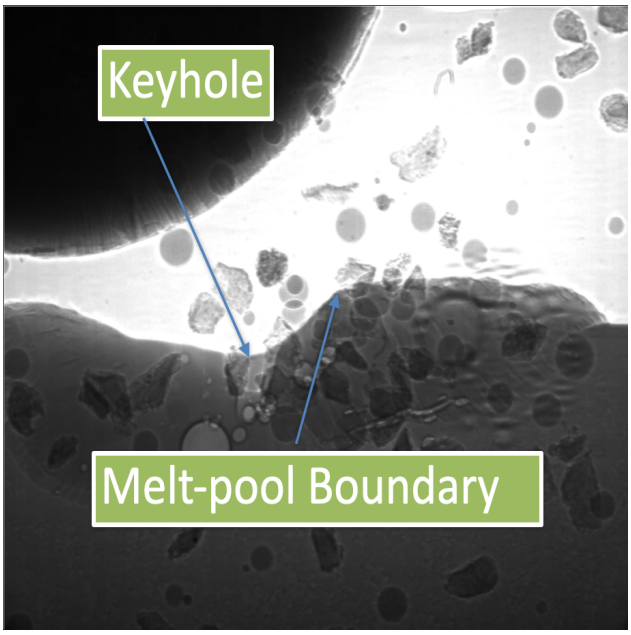

(c) The laser starts to reaches end of the depression region

Figure 3.6: The laser is in the depression region created at the end of first laser pass. This is the time where we see a dip in emissivity which leads to errors while determining the melt pool boundary.

3.4 Conclusion

The change in emissivity between the first and second laser passes was observed using experiments conducted by Dr. Sarah Wolff and her collegues at the Argonne National Laboratory. The emissivity was calculated by using eq. 3.1. The radiometric liquidus temperature was calculated dynamically by extracting the temperature from pixels corresponding to the melt pool boundary leading the laser. A substantial increase in emissivity was noticed during the second laser pass. This must be due to the increase in surface roughness caused by the DED process, as previous research dictates that the emissivity of Ti 6-Al 4-V decreases after a threshold is reached. The emissivity calculated for the first laser pass varies around a mean of 0.045, which is less than half of the values found for T 6-Al 4-V in previous research work by others. This may be due to the high surface finish of the substrate used which increases its reflectivity, thus, decreasing its emissivity. A dip in emissivity was noticed during the beginning of the second laser pass which may be due to a depression in the surface made at the end of the first laser pass. The laser enters this depression and may lead to a reduction in radiation sensed by the IR sensor due to the angle of axis of the IR camera changing with respect to the surface at the point of this depression.

As the laser moves forward the melt pool boundary is masked by the heat radiated due to latent heat of solidification. This gives an incorrect reading for the melt pool boundary which leads to an error in estimating the melt pool for those latter frames.

3.5 Future Work

Filter with a higher temperature range will be used to separate the latent heat solidification from the laser. Further research needs to be done to correlate the melt pool dynamics with the infrared red radiation on the melt pool surface to determine patterns that lead to coalescence in order to control or avoid this phenomenon. Previous research has used machine learning to predict the position of porosity in the final part using infrared radiation as input. However, a causal relationship between in-situ infrared radiation and location of porosity needs to be studied further.

REFERENCES

[1] S. J. Wolff, S. Webster, N. D. Parab, B. Aronson, B. Gould, A. Greco, and T. Sun, "In-situ Observations of Directed Energy Deposition Additive Manufacturing Using High-Speed X-ray Imaging," *Jom*, vol. 73, no. 1, pp. 189–200, 2021.

[2] J. Barrios-Muriel, F. Romero-Sánchez, F. J. Alonso-Sánchez, and D. R. Salgado, "Advances in orthotic and prosthetic manufacturing: A technology review," *Materials*, vol. 13, no. 2, 2020.

[3] W. Zhu, X. Ma, M. Gou, D. Mei, K. Zhang, and S. Chen, "3D printing of functional biomaterials for tissue engineering," *Current Opinion in Biotechnology*, vol. 40, pp. 103–112, 2016.

[4] S. Bose, S. Vahabzadeh, and A. Bandyopadhyay, "Bone tissue engineering using 3D printing," *Materials Today*, vol. 16, no. 12, pp. 496–504, 2013.

[5] J. Goole and K. Amighi, "3D printing in pharmaceutics: A new tool for designing customized drug delivery systems," *International Journal of Pharmaceutics*, vol. 499, no. 1-2, pp. 376–394, 2016.

[6] J. Sun, W. Zhou, D. Huang, J. Y. Fuh, and G. S. Hong, "An Overview of 3D Printing Technologies for Food Fabrication," *Food and Bioprocess Technology*, vol. 8, no. 8, pp. 1605–1615, 2015.

[7] S. Singh, S. Ramakrishna, and R. Singh, "Material issues in additive manufacturing: A review," *Journal of Manufacturing Processes*, vol. 25, pp. 185–200, 2017.

[8] S. Singh, S. Ramakrishna, and R. Singh, "Material issues in additive manufacturing: A review," *Journal of Manufacturing Processes*, vol. 25, pp. 185–200, 2017.

[9] P. F. Jacobs, *Rapid prototyping & manufacturing: fundamentals of stereolithography*. Society of Manufacturing Engineers, 1992.

[10] T. G. Gawel, "Review of Additive Manufacturing Methods," *Solid State Phenomena*, vol. 308, pp. 1–20, jul 2020.

[11] P. Y. Lin, F. C. Shen, K. T. Wu, S. J. Hwang, and H. H. Lee, "Process optimization for directed energy deposition of SS316L components," *International Journal of Advanced Manufacturing Technology*, vol. 111, no. 5-6, pp. 1387–1400, 2020.

[12] S. J. Wolff, H. Wang, B. Gould, N. Parab, Z. Wu, C. Zhao, A. Greco, and T. Sun, "In situ X-ray imaging of pore formation mechanisms and dynamics in laser powder-blown directed energy deposition additive manufacturing," *International Journal of Machine Tools and Manufacture*, vol. 166, no. March, p. 103743, 2021.

[13] G. Tapia and A. Elwany, "A Review on Process Monitoring and Control in Metal-Based Additive Manufacturing," *Journal of Manufacturing Science and Engineering, Transactions of the ASME*, vol. 136, no. 6, pp. 1–10, 2014.

[14] W. L. Wolfe, *The infrared handbook*, vol. 10. The Office, 1978.

[15] C. Cagran, G. Pottlacher, M. Rink, and W. Bauer, "Spectral emissivities and emissivity x-points of pure molybdenum and tungsten," *International Journal of Thermophysics*, vol. 26, no. 4, pp. 1001–1015, 2005.

[16] L. Li, K. Yu, K. Zhang, and Y. Liu, "Study of ti–6al–4v alloy spectral emissivity characteristics during thermal oxidation process," *International Journal of Heat and Mass Transfer*, vol. 101, pp. 699–706, 2016.

[17] B. Gould, S. Wolff, N. Parab, C. Zhao, M. C. Lorenzo-Martin, K. Fezzaa, A. Greco, and T. Sun, "In Situ Analysis of Laser Powder Bed Fusion Using Simultaneous High-Speed Infrared and X-ray Imaging," *Jom*, vol. 73, no. 1, pp. 201–211, 2021.

[18] A. Pinkerton, "Laser direct metal deposition: theory and applications in manufacturing and maintenance," in *Advances in Laser Materials Processing*, pp. 461–491, Elsevier, 2010.

[19] S. Razavi, G. Bordonaro, P. Ferro, J. Torgersen, and F. Berto, "Fatigue Behavior of Porous Ti-6Al-4V Made by Laser-Engineered Net Shaping," *Materials*, vol. 11, p. 284, feb 2018.

[20] A. A. Shatsov, "Mechanical properties of porous materials," *Metal Science and Heat Treatment*, vol. 45, no. 11-12, pp. 441–444, 2003.

[21] A. du Plessis, I. Yadroitsava, and I. Yadroitsev, "Effects of defects on mechanical properties in metal additive manufacturing: A review focusing on X-ray tomography insights," *Materials and Design*, vol. 187, p. 108385, 2020.

[22] S. Ji, Q. Gu, and B. Xia, "Porosity dependence of mechanical properties of solid materials," *Journal of Materials Science*, vol. 41, no. 6, pp. 1757–1768, 2006.

[23] T. Zhao, Y. Wang, T. Xu, M. Bakir, W. Cai, M. Wang, M. Dahmen, Q. Zheng, X. Wei, C. Hong, C. Zhong, P. Albus, T. Schopphoven, A. Gasser, and C. L. Häfner, "Some factors affecting porosity in directed energy deposition of AlMgScZr-alloys," *Optics and Laser Technology*, vol. 143, no. June, 2021.

[24] S. Rhee, "Porosity—Thermal conductivity correlations for ceramic materials," *Materials Science and Engineering*, vol. 20, pp. 89–93, jan 1975.

[25] C. Zhao, K. Fezzaa, R. W. Cunningham, H. Wen, F. De Carlo, L. Chen, A. D. Rollett, and T. Sun, "Real-time monitoring of laser powder bed fusion process using high-speed X-ray imaging and diffraction," *Scientific Reports*, vol. 7, no. 1, pp. 1–11, 2017.

[26] A. Bobel, L. G. Hector, I. Chelladurai, A. K. Sachdev, T. Brown, W. A. Poling, R. Kubic, B. Gould, C. Zhao, N. Parab, A. Greco, and T. Sun, "In situ synchrotron X-ray imaging of 4140 steel laser powder bed fusion," *Materialia*, vol. 6, no. March, 2019.

[27] A. A. Martin, N. P. Calta, J. A. Hammons, S. A. Khairallah, M. H. Nielsen, R. M. Shuttlesworth, N. Sinclair, M. J. Matthews, J. R. Jeffries, T. M. Willey, and J. R. Lee, "Ultrafast dynamics of laser-metal interactions in additive manufacturing alloys captured by in situ X-ray imaging," *Materials Today Advances*, vol. 1, p. 100002, 2019.

[28] C. Zhao, N. D. Parab, X. Li, K. Fezzaa, W. Tan, A. D. Rollett, and T. Sun, "Critical instability at moving keyhole tip generates porosity in laser melting," *Science*, vol. 370, no. 6520, pp. 1080–1086, 2020.

[29] A. Matsunawa, M. Mizutani, S. Katayama, and N. Seto, "Porosity formation mechanism and its prevention in laser welding," *Welding International*, vol. 17, no. 6, pp. 431–437, 2003.

[30] S. M. H. Hojjatzadeh, Q. Guo, N. D. Parab, M. Qu, L. I. Escano, K. Fezzaa, W. Everhart, T. Sun, and L. Chen, "In-situ characterization of pore formation dynamics in pulsed wave laser powder bed fusion," *Materials*, vol. 14, no. 11, pp. 1–11, 2021.

[31] S. A. Khairallah, A. T. Anderson, A. Rubenchik, and W. E. King, "Laser powder-bed fusion additive manufacturing: Physics of complex melt flow and formation mechanisms of pores, spatter, and denudation zones," *Acta Materialia*, vol. 108, pp. 36–45, 2016.

[32] R. Cunningham, C. Zhao, N. Parab, C. Kantzos, J. Pauza, K. Fezzaa, T. Sun, and A. D. Rollett, "Keyhole threshold and morphology in laser melting revealed by ultrahigh-speed x-ray imaging," *Science*, vol. 363, no. 6429, pp. 849–852, 2019.

[33] N. A. Kistler, D. J. Corbin, A. R. Nassar, E. W. Reutzel, and A. M. Beese, "Effect of processing conditions on the microstructure, porosity, and mechanical properties of Ti-6Al-4V repair fabricated by directed energy deposition," *Journal of Materials Processing Technology*, vol. 264, no. February 2018, pp. 172–181, 2019.

[34] Y. Kakinuma, M. Mori, Y. Oda, T. Mori, M. Kashihara, A. Hansel, and M. Fujishima, "Influence of metal powder characteristics on product quality with directed energy deposition of Inconel 625," *CIRP Annals - Manufacturing Technology*, vol. 65, no. 1, pp. 209–212, 2016.

[35] B. Rabin, G. Smolik, and G. Korth, "Characterization of entrapped gases in rapidly solidified powders," *Materials Science and Engineering: A*, vol. 124, pp. 1–7, apr 1990.

[36] K. Kubo and R. D. Pehlke, "Mathematical modeling of porosity formation in solidification," *Metallurgical Transactions B*, vol. 16, no. 2, pp. 359–366, 1985.

[37] S. M. H. Hojjatzadeh, N. D. Parab, W. Yan, Q. Guo, L. Xiong, C. Zhao, M. Qu, L. I. Escano, X. Xiao, K. Fezzaa, W. Everhart, T. Sun, and L. Chen, "Pore elimination mechanisms during 3D printing of metals," *Nature Communications*, vol. 10, no. 1, pp. 1–8, 2019.

[38] Z. jue Tang, W. wei Liu, Y. wen Wang, K. M. Saleheen, Z. chao Liu, S. tong Peng, Z. Zhang, and H. chao Zhang, "A review on in situ monitoring technology for directed energy deposition of metals," *International Journal of Advanced Manufacturing Technology*, vol. 108, no. 11-12, pp. 3437–3463, 2020.

[39] W. Ren, Z. Zhang, Y. Lu, G. Wen, and J. Mazumder, "In-Situ Monitoring of Laser Additive Manufacturing for Al7075 Alloy Using Emission Spectroscopy and Plume Imaging," *IEEE Access*, vol. 9, pp. 61671–61679, 2021.

[40] S. J. Wolff, Z. Gan, S. Lin, J. L. Bennett, W. Yan, G. Hyatt, K. F. Ehmann, G. J. Wagner, W. K. Liu, and J. Cao, "Experimentally validated predictions of thermal history and microhardness in laser-deposited Inconel 718 on carbon steel," *Additive Manufacturing*, vol. 27, pp. 540–551, may 2019.

[41] M. Khanzadeh, S. Chowdhury, M. A. Tschopp, H. R. Doude, M. Marufuzzaman, and L. Bian, "In-situ monitoring of melt pool images for porosity prediction in directed energy deposition processes," *IISE Transactions*, vol. 51, no. 5, pp. 437–455, 2019.

[42] B. T. Gibson, Y. K. Bandari, B. S. Richardson, W. C. Henry, E. J. Vetland, T. W. Sundermann, and L. J. Love, "Melt pool size control through multiple closed-loop modalities in laser-wire directed energy deposition of Ti-6Al-4V," *Additive Manufacturing*, vol. 32, no. November 2019, p. 100993, 2020.

[43] W. Yu, S. L. Sing, C. K. Chua, and X. Tian, "Influence of re-melting on surface roughness and porosity of AlSi10Mg parts fabricated by selective laser melting," *Journal of Alloys and Compounds*, vol. 792, pp. 574–581, 2019.

[44] Y. Liao and D. Lucas, "A literature review on mechanisms and models for the coalescence process of fluid particles," *Chemical Engineering Science*, vol. 65, no. 10, pp. 2851–2864, 2010.

[45] Q. Shen, W. K. Lee, K. Fezzaa, Y. S. Chu, F. De Carlo, P. Jemian, J. Ilavsky, M. Erdmann, and G. G. Long, "Dedicated full-field X-ray imaging beamline at Advanced Photon Source," *Nu-*

clear Instruments and Methods in Physics Research, Section A: Accelerators, Spectrometers, Detectors and Associated Equipment, vol. 582, no. 1, pp. 77–79, 2007.

[46] C.-H. LEE, L. ERICKSON, and L. GLASGOW, "BUBBLE BREAKUP AND COALESCENCE IN TURBULENT GAS-LIQUID DISPERSIONS," *Chemical Engineering Communications*, vol. 59, pp. 65–84, sep 1987.

[47] S. Orvalho, M. C. Ruzicka, G. Olivieri, and A. Marzocchella, "Bubble coalescence: Effect of bubble approach velocity and liquid viscosity," *Chemical Engineering Science*, vol. 134, pp. 205–216, 2015.

[48] S. A. Khairallah, A. T. Anderson, A. Rubenchik, and W. E. King, "Laser powder-bed fusion additive manufacturing: Physics of complex melt flow and formation mechanisms of pores, spatter, and denudation zones," *Acta Materialia*, vol. 108, pp. 36–45, 2016.

[49] P. Rice, *Mechanics and Physics of bubbles liquids*, vol. 26. 1983.

[50] C. A. Coulaloglou and L. L. Tavlarides, "Description of interaction processes in agitated liquid-liquid dispersions," *Chemical Engineering Science*, vol. 32, no. 11, pp. 1289–1297, 1977.

[51] C. A. COULALOGLOU, "DISPERSED PHASE INTERACTIONS IN AN AGITATED FLOW VESSEL,"

[52] P. Coppa and A. Consorti, "Normal emissivity of samples surrounded by surfaces at diverse temperatures," *Measurement: Journal of the International Measurement Confederation*, vol. 38, no. 2, pp. 124–131, 2005.

[53] L. González-Fernández, E. Risueño, R. Pérez-Sáez, and M. Tello, "Infrared normal spectral emissivity of Ti–6Al–4V alloy in the 500–1150K temperature range," *Journal of Alloys and Compounds*, vol. 541, pp. 144–149, nov 2012.

[54] H. Watanabe, M. Susa, H. Fukuyama, and K. Nagata, "Phase (Liquid/Solid) Dependence of the Normal Spectral Emissivity for Iron, Cobalt, and Nickel at Melting Points," *International Journal of Thermophysics*, vol. 24, no. 2, pp. 473–488, 2003.

[55] H. J. Jo, J. L. King, K. Blomstrand, and K. Sridharan, "Spectral emissivity of oxidized and roughened metal surfaces," *International Journal of Heat and Mass Transfer*, vol. 115, pp. 1065–1071, 2017.

[56] J. L. King, H. Jo, R. Tirawat, K. Blomstrand, and K. Sridharan, "Effects of surface roughness, oxidation, and temperature on the emissivity of reactor pressure vessel alloys," *Nuclear Technology*, vol. 200, no. 1, pp. 1–14, 2017.